

A Study of the Infrared Emission Line Structure of HH 7-11 with *Hubble* and *Spitzer*

Natalie Allen

Abstract

We present new Hubble Space Telescope (HST) observations of the HH 7-11 outflow region. We use the near-infrared [Fe II] pair to find the extinction towards the emission, giving a quasi-3D picture of the outflow's deposition of momentum and heat into the surroundings. We also use the shock simulation program MAPPINGS V to find initial parameters of this outflow and the shocks it forms and determine the amount of energy and momentum being deposited from this shock into the cloud.

A thesis submitted to the Department of Physics and Astronomy gaining a full enrichment of the bachelor's degree. Supervised by Professor Dan Watson.



UNIVERSITY *of*
ROCHESTER

Department of Physics and Astronomy
University of Rochester
Rochester, New York
2020

1. INTRODUCTION

We observe young stars to rotate rather slowly, but the angular momentum received by the star during the accretion process that forms them is large and ever growing. For the young star to not be disrupted by the increasing torque from this angular momentum, some of the excess angular momentum must be removed. In the last few decades, it has become clear that the carrier of surplus angular momentum is an outflow, in most cases bipolar, and oriented along the system rotational axis (for an overview, see [Bally 2016](#)). First found in CO in the 1970s ([Wilson et al. 1970](#)) and mapped in ever-increasing detail in the decades since as technology has improved, molecular outflows have now been observed and theorized to be ejected from many, if not all, young stars. The models that best describe these outflows are magnetocentrifugal in nature, owing to the freezing of magnetic field lines onto the rotating core or inner disk ([Frank et al. 2014](#)). Images of outflows provide a history of past ejections and thus can trace back to the mass accretion rates of forming stars, as well as allow for a possible determination of their natal cloud's future through their momentum and energy injection rates.

When these outflows leave the protostellar core, they travel tens to hundreds of kilometers per second, and the outflow collides supersonically with the material surrounding the star. The resulting shocked gas emits brightly in low-excitation ionic and molecular lines, appearing as visible/infrared Herbig-Haro (HH) objects, and bipolar structures in the high-velocity wings of millimeter-wave molecular lines. Depending on the characteristics of the outflow, the shocks can be categorized as either J-type (jump) or C-type (continuous) as defined and described in [Draine \(1980\)](#). As can be understood by their names, in J-type shocks the parameters undergo a "jump" and are discontinuous at the jump front, while in a C-type shock the parameters are continuous through the shock. J-type shocks tend to be faster than their C-type counterparts, and may dissociate molecules during their passage.

Both types have been used to model HH objects in the past, and are believed to map different parts of the shock.

NGC 1333 is likely the most protostar and outflow rich molecular cloud in the nearest few hundred parsecs ($d \sim 300$ pc, see [Zucker et al. 2018](#); [Hartigan et al. 2019](#)). The molecular cloud associated with NGC 1333 is of modest size ($\sim 350 M_{\odot}$); background-star colors indicate visual extinctions ranging over 2-24 magnitudes. In [Figure 1](#), NGC 1333 is shown in visible light, an extinction map, and in infrared to illustrate the significant dust and extinction present in the region and the effect that has on observations. A considerable number of surveys, including the infrared Spitzer image included in [Figure 1](#), have covered this field. This region is quite young as star-formation regions go: many of its associated objects are Class 0 and 1 protostars - those that still have their envelopes. As these are the stars in their main accretion stage, many currently have outflows, and so it is home to a significant number of HH objects. [Reipurth \(1991\)](#) counted 36 HH objects in this region, and a considerable amount have been discovered since (e.g. [Walawender et al. 2005](#)). It is home to several of the brightest HH objects in the sky, including the HH 7-11 chain. These were among the first Herbig Haro objects to be discovered ([Herbig 1974](#)), and remain one of the best studied examples of this phenomenon. The outflow's source is one of the components of the multiple protostar SVS 13A ([Strom et al. 1976](#); [Rodríguez et al. 1997](#); [Anglada et al. 2000](#); [Hodapp & Chini 2014](#)). We will refer to the source as SVS 13 henceforth.

Proper motions of HH 7-11 have been measured in the infrared by [Khanzadyan et al. \(2003\)](#) and [Raga et al. \(2013\)](#) and in the optical by [Herbig & Jones \(1983\)](#), [Noriega-Crespo & Garnavich \(2001\)](#), and [Hartigan et al. \(2019\)](#). While the values differ, the general consensus seems to be (using $d = 300$ pc) $\sim 20 - 40$ km/s for HH 7 and $\sim 75 - 100$ km/s for HH 11. The values for the inner HH objects are contested, with proper motions around $12 - 30$ km/s found by [Raga et al. \(2013\)](#) and [Noriega-Crespo & Garnavich \(2001\)](#), but essentially none found by [Hartigan et al. \(2019\)](#). These objects have also had their radial velocities measured by [Solf & Böhm \(1987\)](#), which reports that all objects are blueshifted, with HH 7-10 having a uniform radial velocity of ~ -50 km/s but HH 11 having a much larger radial velocity of ~ -200 km/s.

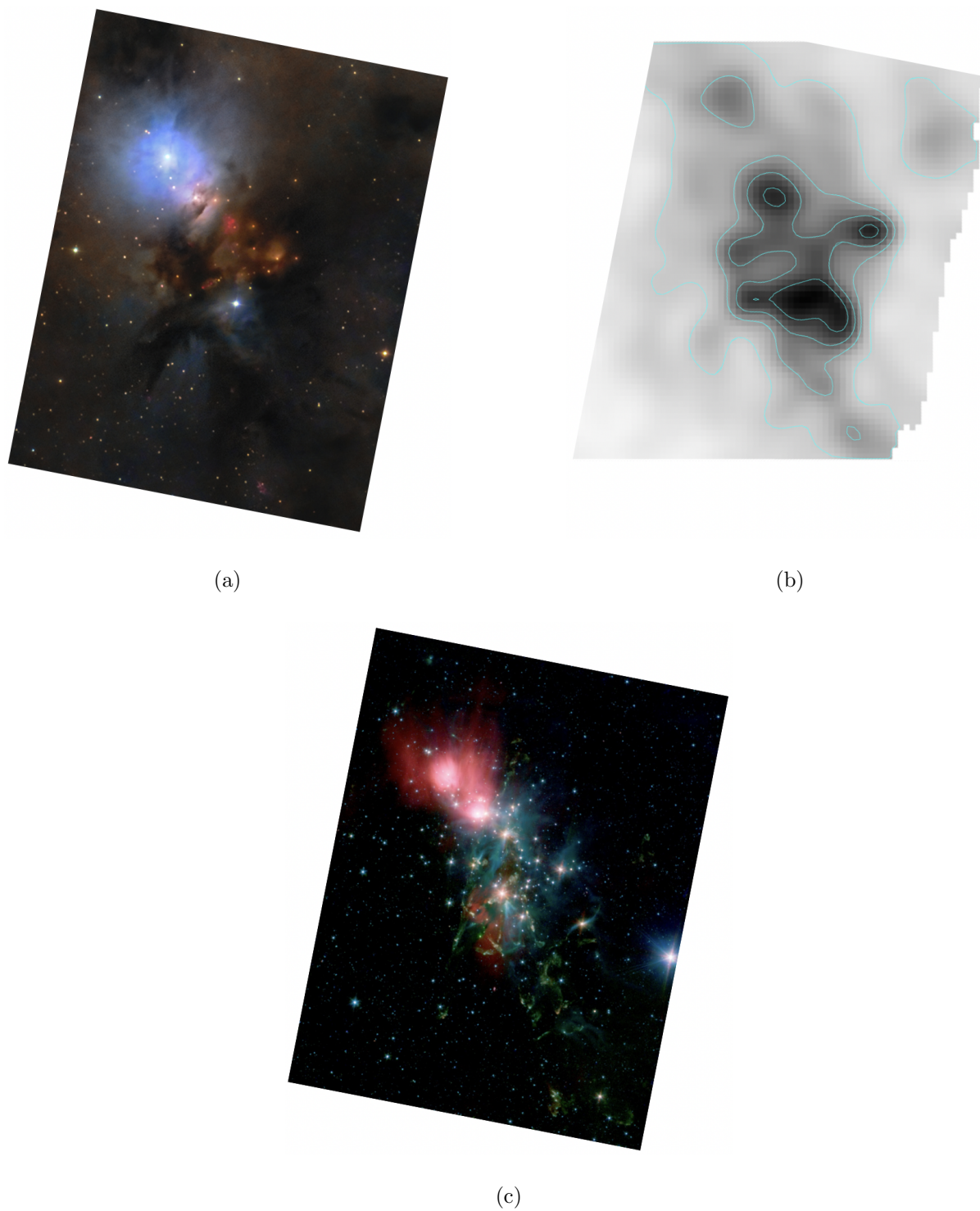


Figure 1. a: A visible light image of NGC 1333, taken by Lorand Fenyés (2017). b: An extinction map of NGC 1333, with contours at 5, 10, 15, 20, and 25 magnitudes (Gutermuth et al. 2008), measured from near-infrared color excess of background stars. c: Spitzer IRAC mosaics of NGC 1333; 3.6, 4.5, and 8.0 μm images mapped to blue, green, and red, respectively (Gutermuth et al. 2008).

To look at star formation regions that are likely to be heavily extinguished due to the large amount of dusty gas that is causing the formation in the first place, use of infrared light is optimal. It allows a view past the dust into the heart of the cloud where the formation is taking place, and also allows for a view of the emission that is less energetic than would be visible in optical even if one could see through the dust. Yet it still allows the observer to probe high-excitation sectors of the shocked gas. The high resolution afforded by the Hubble Space Telescope (HST) in the near-infrared allows us to ask questions about the morphology in the region and the physical processes behind them at in great detail. Although ground based adaptive optics (AO) achieves higher resolution than HST at some wavelengths, the requirement of an optically bright guide star makes it difficult to use for large extended objects or in regions of large extinction. In addition, the resolution of HST is diffraction limited and can cover an area of several arcminutes with this clear resolution. For regions like HH 7-11, which cover areas of almost 100 arcseconds, observations made with HST are clearer. In the mid infrared, the Spitzer Space Telescope offers another important view, even freer of extinction though with lower angular resolution. The NIRCAM/NIRSPEC ($0.6 - 5 \mu\text{m}$) and MIRI ($4.9 - 28.8 \mu\text{m}$) instruments on the upcoming *James Webb Space Telescope* will be excellent at observing these types of star formation regions in the future (Gardner et al. 2006).

Here we present new high spatial resolution infrared spectral-line imaging observations of SVS 13 and its associated outflow, including HH 7-11 and the heavily-extinguished counterjet, in the spectral lines [Fe II] $1.26 \mu\text{m}$ and $1.64 \mu\text{m}$ [Fe II], and H I Pa β . We use these observations, along with some of our previous observations with Spitzer-IRS, in an analysis of the three-dimensional structure of the outflow and its interaction with its surroundings, and the physical state of the outflowing and shocked gas. The details of our observations and data reduction techniques are given in Section 2, along with the rest of the data that will be used against the new observations for the study of the region. Following are high resolution morphological arguments in Section 3. Analysis is given in Section 4, including a determination of the extinction towards the objects in 4.1 and a comparison of this observational data with that predicted by the shock model MAPPINGS V in Section 4.2, along

with what that can tell us about larger scale structure in 4.3. We conclude with our results in Section 5.

2. OBSERVATIONS

Observations of NGC 1333 were carried out from January to February 2018 with the Hubble Space Telescope and Wide Field Camera 3, under General Observing Proposal 15153 (D. Watson, PI). The region was imaged in 3 wavelengths using WFC3/IR: 1.26 μm (F126N) and 1.64 μm (F164N) [Fe II] and 1.28 μm (F164N) H I Pa β .

Of the 33 program orbits, 27 were used to image 64 slightly overlapping fields in each of the three wavelengths using Drift-and-Shift (DASH) mode (Momcheva et al. 2017). In this mode the observing efficiency is improved dramatically over startracker-guided observations, permitting us to cover a field about half the size of the Moon in three infrared narrowband filters in only 27 HST orbits. Together, these 64 frames encompass most of the NGC 1333 cloud as imaged with the Spitzer Space Telescope as reported by Gutermuth et al. (2008), and shown in Figure 1. Observations were taken in strips of 8 fields per visit. While the first frame in each strip of observations is reliably close to the requested and reported world coordinate system (WCS), due to the novel observing technique many of the subsequent observations in the series suffered from significant drift and caused the reported WCS coordinates of the images to be far from where they actually fell. This drift became more severe the longer it occurred after the original aligning of the orbit took place. Thus, the basic WFC3 pipeline was not sufficient to prep the images for analysis. Instead, the locations of the images were corrected by matching the WCS coordinate position of the centroids of stars visible in each frame with those of stars from the Two Micron All Sky Survey (2MASS) (Skrutskie et al. 2006), where possible. These positions were further corrected by using the TweakReg task from the DrizzlePac software (Gonzaga et al. 2012) to align the centroids of common stars between frames. The images were then mosaicked together using the AstroDrizzle task, also from DrizzlePac, to create a final large scale mosaic of the region. During the drizzling process, the sky subtraction method globalmin was used as the default method localmin left visible artifacts. The rest of the parameters were used as standard. Only the regions in the direct vicinity of HH 7-11 and the area directly opposite it behind SVS 13 will be

analyzed in this paper; the rest of the mosaic will be covered in subsequent papers. The full mosaic is shown in Figure 2.

The other 6 orbits were used for deep exposure, startracker guided images in the same three wavelengths of regions of particular interest in the middle of the cloud, centered on HH 7-11 and regions nearby. Each frame was revisited 4 times for each wavelength. These observations also suffered from significant drift in subsequent observations due to loss of guide star, which caused the reported WCS coordinates in the headers to be wrong. The same strategy of alignment with 2MASS and then using the TweakReg task was used to align these frames to each other. Since there were multiple observations of the same frame in each wavelength, these were stacked together using Astrodrizzle after alignment to obtain more flux in addition to a more complete removal of rogue pixels. The same parameters as used for the DASH mode drizzling was used here. The rogue pixels were not completely corrected for in the $1.28 \mu\text{m}$ frames, likely due to filter effects. Thus, to further clean the images, a search was done for each pixel that had a large value in comparison to its nearest neighbors (essentially a k-nearest neighbors algorithm). If one of these pixels was found, it was smoothed over by averaging the pixels surrounding it and replacing its pixel value with that average value instead.

To calibrate the data, the pixel values were collected in counts using the IDL task ATV (Barth 2001) for the stars available in the frames. First, they were compared to the values observed by 2MASS. Each line was isolated by a narrowband filter built into WFC3. The $1.26 \mu\text{m}$ [Fe II] was compared to J magnitude (centered at $1.25 \mu\text{m}$), and $1.64 \mu\text{m}$ [Fe II] was compared to H magnitude (centered at $1.65 \mu\text{m}$), which were converted from magnitudes to flux density in Janskys using the reported zero magnitude values (Cutri et al. 2006). These were found to be in good agreement (4% for $1.26 \mu\text{m}$ and 15% for $1.64 \mu\text{m}$), and thus the values from the header could reliably be used to convert the pixel values to line flux. As stated in the FITS file headers, the pixel values are given in electrons/s after going through the DrizzlePac pipeline. For morphology and extinction arguments and calculations, the electrons/s are divided by the integrated system throughput for each filter as reported in Dressel et al. (2019), which accounts for differences due to the filters. To compare the

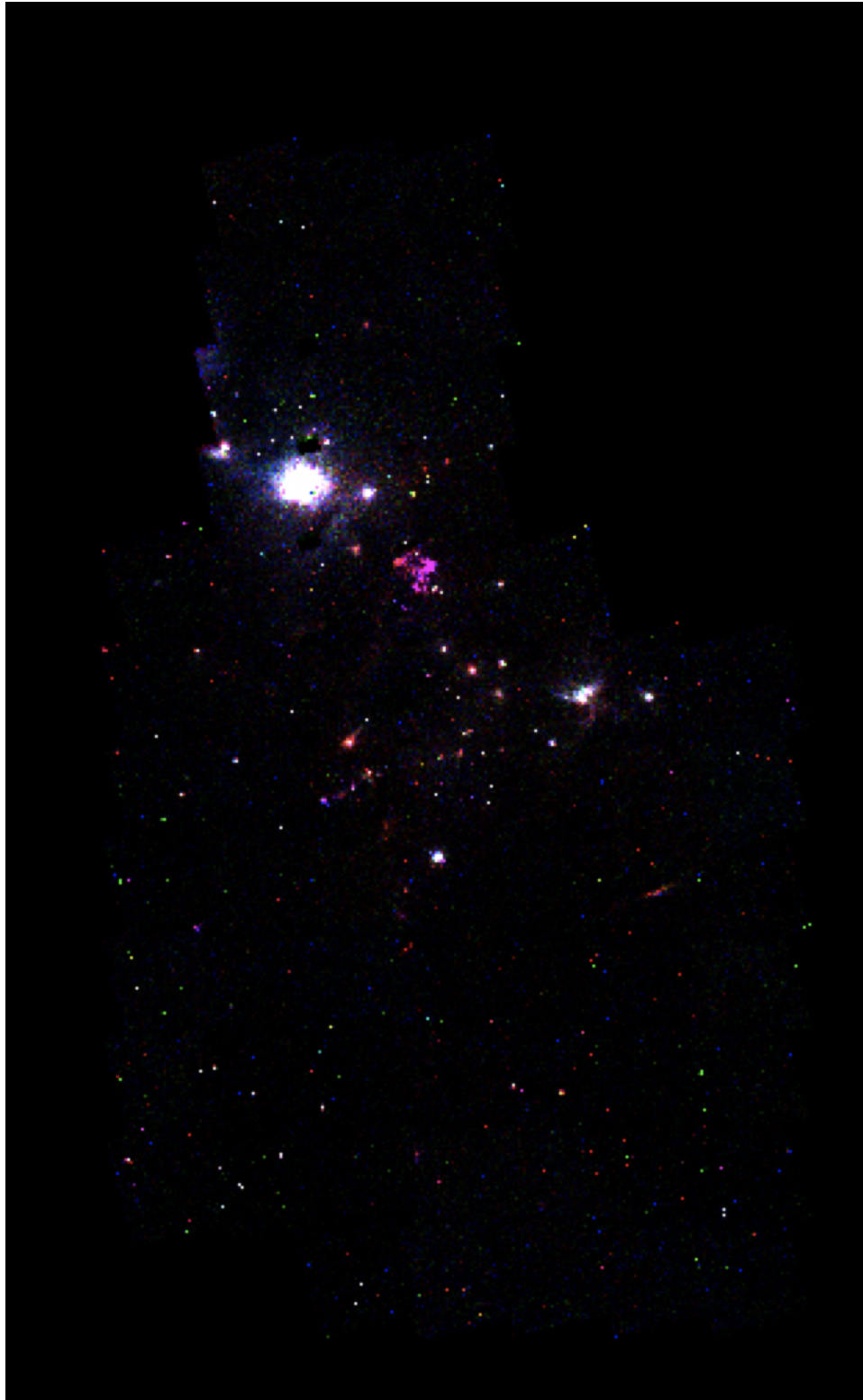


Figure 2. Full mosaic of 64 frames in three wavelengths - $1.64 \mu\text{m}$ (red) [Fe II], $1.28 \mu\text{m}$ HI Pa β (green), $1.26 \mu\text{m}$ [Fe II] (blue) covering 123×136 arcseconds.

observations to models, they need to be converted from counts to physical units. This conversion also corrects for any differences in efficiency for the different filters without having to divide by the throughput, as the effect is included in the conversion factors. This pixel value in counts is multiplied by the PHOTFLAM value from the header, which is the inverse sensitivity given in $\text{ergs}/\text{cm}^2/\text{A}/e-$, then multiplied by the PHOTBW value, which is the RMS bandwidth of the filter plus the detector, to give a normalized line flux in units of $\text{ergs}/\text{cm}^2/\text{s}$.

Our mid-infrared spectral images come from the Spitzer Space Telescope’s Infrared Spectrograph (IRS; Houck et al. 2004). We compiled the final pipeline version (S18.18), basic calibrated data products from programs 113 (G. Melnick, PI), 116 (C. Lawrence), 20378 (E. Bergin), and 30167 (D. Neufeld). All observations took place during 2004-2007. The SVS13A outflow region is a small part of the coverage of programs 116 and 20378, which surveyed most of the NGC 1333 cloud in each IRS spectral module. For the wavelength range $\lambda = 10 \mu\text{m} - 37 \mu\text{m}$ the field was covered by IRS short wavelength, high resolution (SH) and long-wavelength, high-resolution (LH) observations. These modules have resolving power $\lambda/\Delta\lambda \approx 600$. For $\lambda = 5 \mu\text{m} - 38 \mu\text{m}$ we also have IRS long-wavelength, low-resolution (LL) and short-wavelength, low-resolution (SL) observations covering the field, for which the spectral resolving power varies from $\lambda/\Delta\lambda \approx 60$ to $\lambda/\Delta\lambda \approx 120$ at the short- and long-wavelength ends respectively. The SL, SH, and LH observations have been described previously by Maret et al. (2009) and Neufeld et al. (2006, 2007).

All observations included pointing pickup via either the IRS Pickup Cameras or the facility Pointing Calibration and Reconstruction Sensor (PCRS). The accuracy of reconstructed positions, validated by checking the bright continuum sources covered in the maps, is much less than the pixel size in all cases. Spectral images were made by stepping the telescope in the direction perpendicular to the fixed-position slits of each spectrograph. In the LL observations of program 116, the step size was the two-pixel slit width, resulting in a “corrugation” artifact that was fit and removed in later processing. In all other observations the step size was half the slit width, and no such artifact appeared.

To take advantage of improvements in S18.18 data products over previous versions, we re-reduced all previously existing IRS datacubes. For this we used CUBISM (Smith et al. 2007), extracting images of unresolved spectral features at the wavelengths of the spectral lines of the brighter mid-infrared ionic, atomic, and molecular lines expected from shocks in molecular clouds. Usually the signal-to-noise ratio is largest, and the level of remaining artifacts smallest, in SH and LH observations. A few spectral lines suffer from unfortunately-placed, permanently bad pixels in the SH and LH detector arrays, in which case we resort to SL or LL observations. One line affected in this way is $H_2 v = 0$ S(1) at $\lambda = 17.0\mu\text{m}$. The spectrophotometric accuracy of these results, validated by measurement of differences between low-resolution and high-resolution observations, is about 25%.

The result is the first complete Spitzer-IRS datacube of the SVS13A/HH 7-11 outflow. Some of the results have been described previously by Neufeld et al. (2006), Maret et al. (2009), and Yuan & Neufeld (2011).

We supplemented this with data from HST Proposal 15257 (P. Hartigan, PI) taken with WFC3/UVIS on HST, as published in Hartigan et al. (2019) but reprocessed in Astrodrizzle using the same method as described above, $H_2 2.12 \mu\text{m}$ data from the UKIDSS Galactic Plane Survey taken with the United Kingdom Infrared Telescope (UKIRT), and data from HST Proposal 12514 imaged with the Advanced Camera for Surveys Wide Field Channel (ACS/WFC) as was processed by the European Space Agency for press release (ESA/Hubble & NASA, K. Stapelfeldt). The details of all the data used are given in Table 1.

Table 1. Journal of Observation

Observation ID/						Exposure
AOR Key ^a	Date	Telescope	Instrument	Filter ^b	Line(s) Observed	Time (s)
idn125020 ^c	2018 Jan 07	HST	WFC3/IR	F164N	[Fe II] 1.644 μm	1212
idn127020 ^c	2018 Jan 09	HST	WFC3/IR	F126N	[Fe II] 1.257 μm	1212
idn129020 ^c	2018 Jan 17	HST	WFC3/IR	F128N	H I Pa β 1.282 μm	1212

Table 1 continued on next page

Table 1 (*continued*)

Observation ID/ AOR Key ^a	Date	Telescope	Instrument	Filter ^b	Line(s) Observed	Exposure Time (s)
idgi01010 ^d	2017 Dec 24	HST	WFC3/UVIS	F656N	H α .656 μ m	5778
idgi04010 ^d	2017 Dec 11	HST	WFC3/UVIS	F850LP	SDSS z' (Continuum)	2725
idgi05010 ^d	2018 Jan 12	HST	WFC3/UVIS	FQ672N	[Si II] .671 μ m	5778
jpbj01011 ^e	2011 Dec 25	HST	ACS/WFC	F606W	Broad V Filter	1320
jpbj01021 ^e	2011 Dec 25	HST	ACS/WFC	F814W	Broad I Filter	840
5004288 ^f	2004 Feb 28	Spitzer	IRS	SL, SH, LH	...	1970
5004544 ^f	2004 Feb 29	Spitzer	IRS	SL, SH, LH	...	3146
12649472 ^g	2004 Feb 15	Spitzer	IRS	SL, SH, LH, LL	...	10243
12649472 ^g	2004 Feb 16	Spitzer	IRS	SL, SH, LH, LL	...	10246
14585600 ^h	2006 Mar 10	Spitzer	IRS	SH	...	3402
14583808 ^h	2006 Mar 11	Spitzer	IRS	SL, SH	...	10395
14586112 ^h	2006 Mar 12-13	Spitzer	IRS	SL, SH, LH	...	37705
14584320 ^h	2006 Sept 12	Spitzer	IRS	SH	...	3402
14587904 ^h	2006 Sept 15-16	Spitzer	IRS	SL, SH	...	10294
17857024 ⁱ	2007 Oct 1	Spitzer	IRS	LH	...	27456
UKIDSS ^j	2007 Jan 01	UKIRT	WFCAM	H ₂ 1-0 S1	H ₂ 2.12 μ m	21

^aObservation ID is given for HST observations and AOR key is given for Spitzer observations.

^bSH - Short-High, SL - Short-Low, LH - Long-High, LL - Long-Low

^cHST Proposal 15153, PI Dan Watson

^dHST Proposal 15257, PI Pat Hartigan

^eHST Proposal 12514, PI Karl Stapelfeldt

^fSpitzer Program ID 113, PI Gary Melnick

^gSpitzer Program ID 116, PI Charles Lawrence

^hSpitzer Program ID 20378, PI Edwin Bergin

ⁱSpitzer Program ID 30167, PI David Neufeld

^jTaken from the publicly available UKIDSS data, PI Andy Lawrence

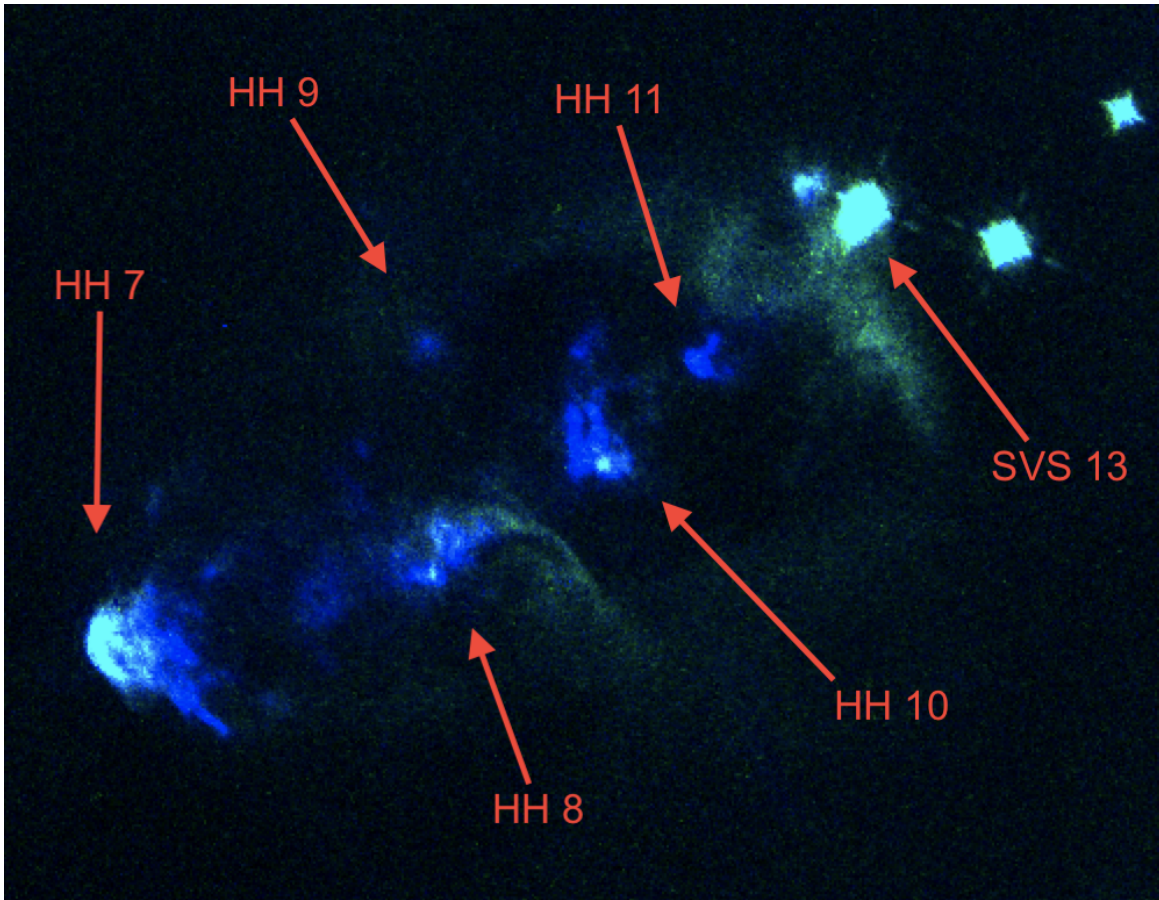


Figure 3. SVS 13 and the associated outflow HH 7-11. Green is the $1.28 \mu\text{m}$ H I Pa β and blue is the $1.26 \mu\text{m}$ [Fe II]. The objects as referred to in this paper are listed.

3. HH 7-11 REGION

We present the new HST image of HH 7-11 in Figure 3 from the deep exposure fine guiding observations. $1.26 \mu\text{m}$ [Fe II] and $1.28 \mu\text{m}$ Pa β are shown, but the $1.64 \mu\text{m}$ [Fe II] line is excluded as it traces precisely the same positions as $1.26 \mu\text{m}$ but with worse image resolution due to the telescope’s diffraction limited nature (shorter wavelengths have higher resolution when diffraction is the limiting factor). This allows us to study small length scales (5×10^{14} cm in the region). We compare the new HST data with the similarly high resolution $0.656 \mu\text{m}$ H α $0.672 \mu\text{m}$ [S II] HST data from Hartigan et al. (2019) and the $2.12 \mu\text{m}$ H_2 from UKIDSS as well for a more in-depth view. $0.672 \mu\text{m}$ [S II] with $1.26 \mu\text{m}$ [Fe II] can be seen in Figure 4 and $0.656 \mu\text{m}$ H α and $2.12 \mu\text{m}$ H_2 can be seen with $1.28 \mu\text{m}$ Pa β in Figure 5.

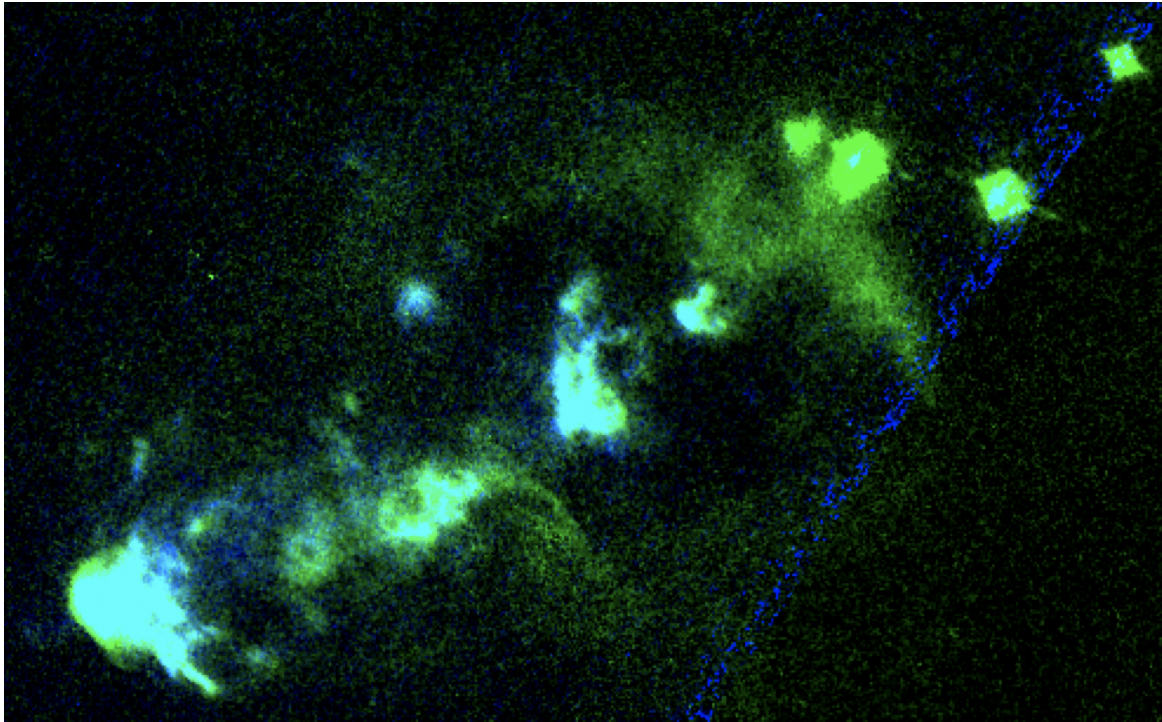


Figure 4. The same region as Figure 3, but with $1.26 \mu\text{m}$ [Fe II] (green) and $0.672 \mu\text{m}$ [S II] (blue).

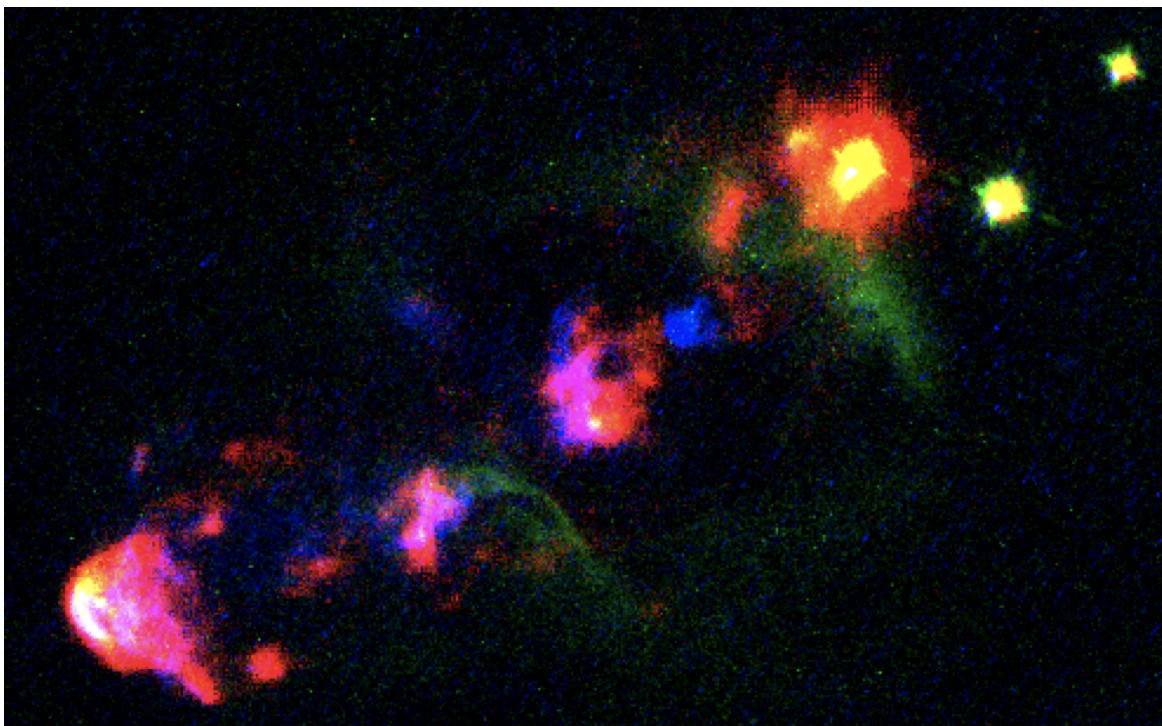


Figure 5. The same region as Figure 3, but with $2.12 \mu\text{m}$ (red), $1.28 \mu\text{m}$ Pa β (green) and $0.656 \mu\text{m}$ H α (blue).

3.1. High Resolution Morphology

3.1.1. HH 7

HH 7, shown in Figure 6, is composed of two main parts: a forward emission knot in the form of a bow shock (A), and a rear emission knot (B). The apex of the object has strong emission from all three emission lines, and the peak of emission strength appears to be the same as well, just about an arcsecond behind the front of the emission. The $\text{Pa}\beta$ emission falls off rather quickly as the object is followed east. Around 3 arcseconds behind the front there seems to be a break in the structure, which is then followed by the rear emission knot B. Right before this break is an especially bright clump of $\text{Pa}\beta$, and there is some $\text{Pa}\beta$ emission that seems to be bridging the break in $[\text{Fe II}]$. This region B is strong and visible in $[\text{Fe II}]$ but much more tenuous in the $\text{Pa}\beta$ emission and doesn't seem to exhibit a front. Both lines do show disruption in the middle of the structure though, just with that in $[\text{Fe II}]$ being more regularly structured. The front is smooth and regular in $[\text{Fe II}]$ for both, and for region A in $\text{Pa}\beta$, although the impact angle appears to be changing in $[\text{Fe II}]$ for the two emission regions. HH 7 ends with "glass fragments" behind the front emission knot that are bright in $[\text{Fe II}]$ and look like they are splashing back from the motion of HH 7.

In $\text{H}\alpha$, both emission regions A and B are visible, although most of the emission in A is behind the front of that seen in the other lines. It is also quite a bit thinner and doesn't span the entire region for A. In B, it is essentially in the same spots as $\text{Pa}\beta$, but continues into some of the fragmentary pieces of $[\text{Fe II}]$ seen east from the main structure. $[\text{S II}]$ falls in essentially the same location as $\text{H}\alpha$ over the entire object, besides having a little less structure in the fragmentary section furthest east. Thus it essentially lies in the same place as $[\text{Fe II}]$, but with a thinner front like $\text{H}\alpha$. In H_2 , the B emission knot is not visible at all. There is just one large shock that encompasses the full space of A and B, with by far the strongest emission in just location A. There is a cavity behind this emission, however, that almost looks like it could be where region B is impacting in the other lines. The clump of $\text{Pa}\beta$ visible behind the front in Figure 6 lines up quite well with the back of the H_2 emission. This is visualized in Figure 6.c and d. Shocks exert the strongest forces near their flow axis (Offner et al. 2011), so it is possible this structure suggests the bow of HH 7 lies closer to the flow axis while

front B lies further away (3 dimensionally). This would explain why the strongest emission is in front A while these high energy tracers are mostly absent from B. The H_2 emission follows the most significant of the fragments, the one to the southwest of the main structure, as well.

3.1.2. *HH 8*

HH 8, shown in Figure 7, appears very differently in $\text{Pa}\beta$ in comparison to $[\text{Fe II}]$. In $\text{Pa}\beta$, the object looks compact and close to HH 10 (A) with just a few bright clumps and a tail flowing east then southeast of the main structure (C). Neither B nor C seem to be very visible in other reported data. However, when viewed in $[\text{Fe II}]$, in addition to being present in the same areas as $\text{Pa}\beta$, the object is much larger, more diffuse, and reaches almost all the way to HH 7. It reaches over more north at the same time, which leads it to span the back of HH 7 almost entirely (B). This can be seen clearly in Figure 3. This is not due to extinction of the $1.28 \mu\text{m}$ $\text{Pa}\beta$ line, as the $1.26 \mu\text{m}$ $[\text{Fe II}]$ line is still strong.

As stars are emitting in hydrogen lines, we must be careful that the $1.28 \mu\text{m}$ $\text{Pa}\beta$ emission is actually emission and not reflected starlight. This is especially important in the case of section C, as it can be seen in Figure 8 that HH 8 seems to lie right on the edge of a large cavity. Inside the cavity is devoid of gas and dust, but the rim on which HH 8 C is has lots of dust and significant reflected light on it. Thus, we compare the deep exposure $\text{Pa}\beta$ image with continuum image taken with WFC3/UVIS filter F850LP (SDSS z' filter) and do see similarities between the locations of the emission. This is shown in Figure 9, and the continuum contamination is taken into account in Section 4.1.

$\text{H}\alpha$ is bright in the same location as $\text{Pa}\beta$ in this object (A), but it stops before B and is not present in the tail C. $[\text{S II}]$ is in the same general area as $\text{H}\alpha$ here, but is significantly more diffuse and only has a few spots of meaningful structure. This seems to be the only place where $[\text{Fe II}]$ and $[\text{S II}]$ have significant difference in their structure. H_2 has emission in this same spot on the main line as $[\text{Fe II}]$ and $[\text{S II}]$, although from a larger area, and is leading the most powerful part of the shock in region A.

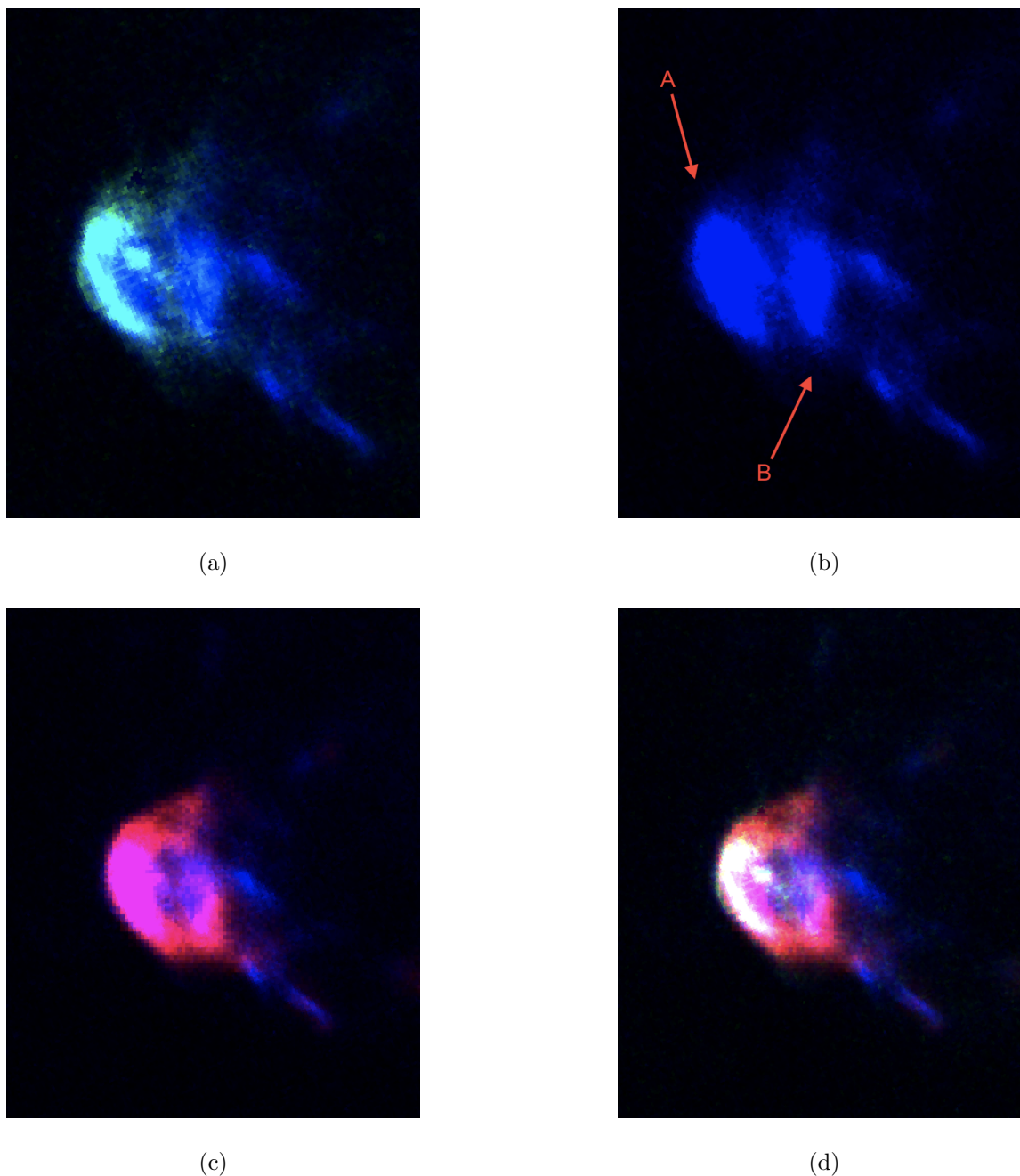


Figure 6. a: HH 7 shown in [Fe II] $1.26 \mu\text{m}$ (blue) and H I $\text{Pa}\beta$ $1.28 \mu\text{m}$ (green). b: HH 7 in just [Fe II] $1.26 \mu\text{m}$, which shows the multiple fronts: the forward front A and the rear front B. The angle of impact seems to be changing between the two regions, with front A pointing further downwards. c: HH 7 shown in H_2 $2.12 \mu\text{m}$ (red) and [Fe II] $1.26 \mu\text{m}$ (green). Both fronts A and B are only seen in [Fe II], with only front A seen in H_2 . However, the back of front A in H_2 seems to have a cavity in the back that might correspond to the impact of front B. d: Same image as c, but with the addition of the $1.28 \mu\text{m}$ $\text{Pa}\beta$. The bright clump of $\text{Pa}\beta$ right behind the shock front lines up well with the back line of the H_2 shock front.

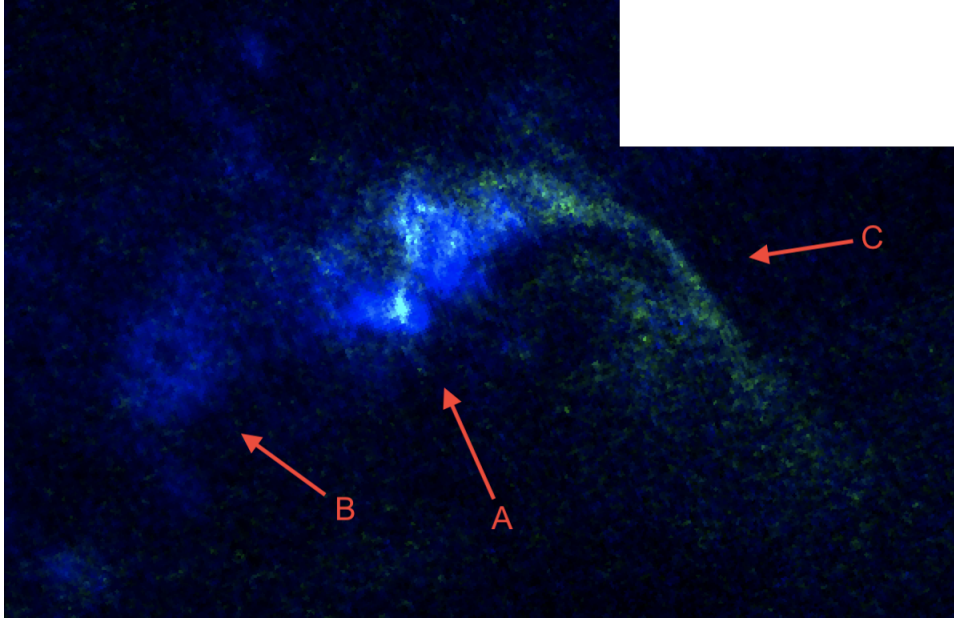


Figure 7. HH 8 shown in [Fe II] 1.26 μm (blue) and Pa β 1.28 μm (green). Three parts of the structure are identified: the main compact object visible in all three lines (A), broad and diffuse [Fe II] emission heading towards HH 7 (B), and a tail leading off behind the main line (C).

3.1.3. *HH 9*

HH 9 is fainter than the others, and is clearly off the main line of visible outflow composed of the other HH objects. There seems to be no emission in Pa β , but relatively strong emission from [Fe II]. The lack of Pa β emission likely means that this portion of the shock was much weaker than what affected the main shock area further south as Pa β is the highest energy tracer. There does look to be a visible stream in all three lines connecting material from around the star to the region of HH 9, which is visible in 3 and 8. It seems to be opposite the tail of HH 8, on the edge of the same cavity. The large amount of dust present in this area likely causes large amounts of extinction, and so the small structure may be due to this. There is no H α or H_2 emission. [S II] does have significant emission though, in the same spot as [Fe II].

3.1.4. *HH 10*

HH 10 is shown in Figure 10. The only Pa β emission seen in HH 10 is along the line of what seems to be the most collimated shock (A), which lines up with HH 11, the main part of HH 8, and then

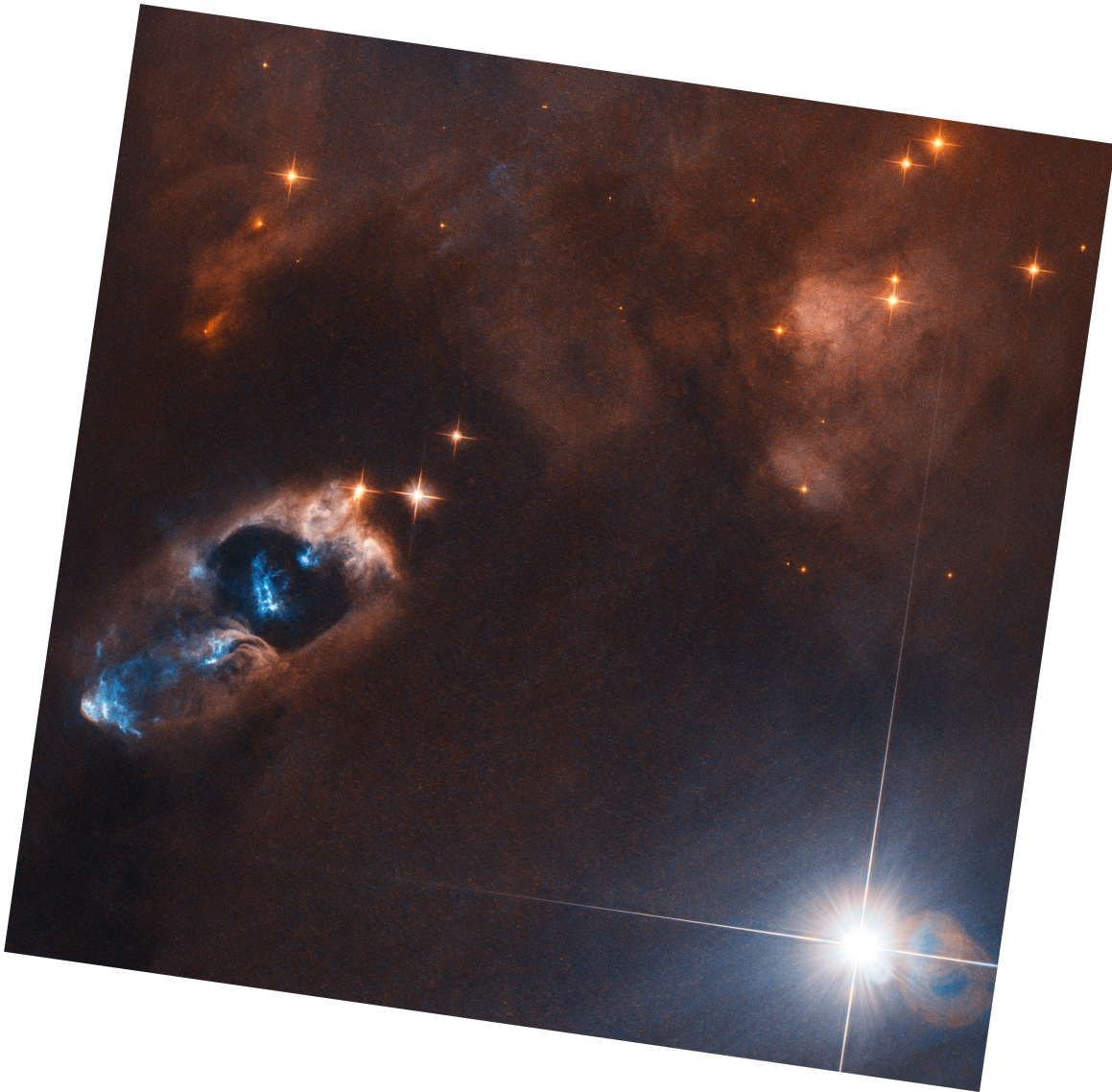


Figure 8. HH 7-11 shown in continuum emission, processed for press release. Image credit: ESA/Hubble & NASA, K. Stapelfeldt

culminates in HH 7. As $\text{Pa}\beta$ is the highest energy tracer in this data, the fact that this emission seems to create a more compact structure may mean that it lies along the strongest shock coming from SVS 13. This would mean that the most energetic shock is thin, and that the angle becomes wider as the shocks become less powerful, similar to the same example of this possibility seen in the two fronts of HH 7. The $[\text{Fe II}]$ emission is much more diffuse and widespread (B), with emission going almost all the way south to the other side of the full outflow region, to where HH 9 is. HH 10

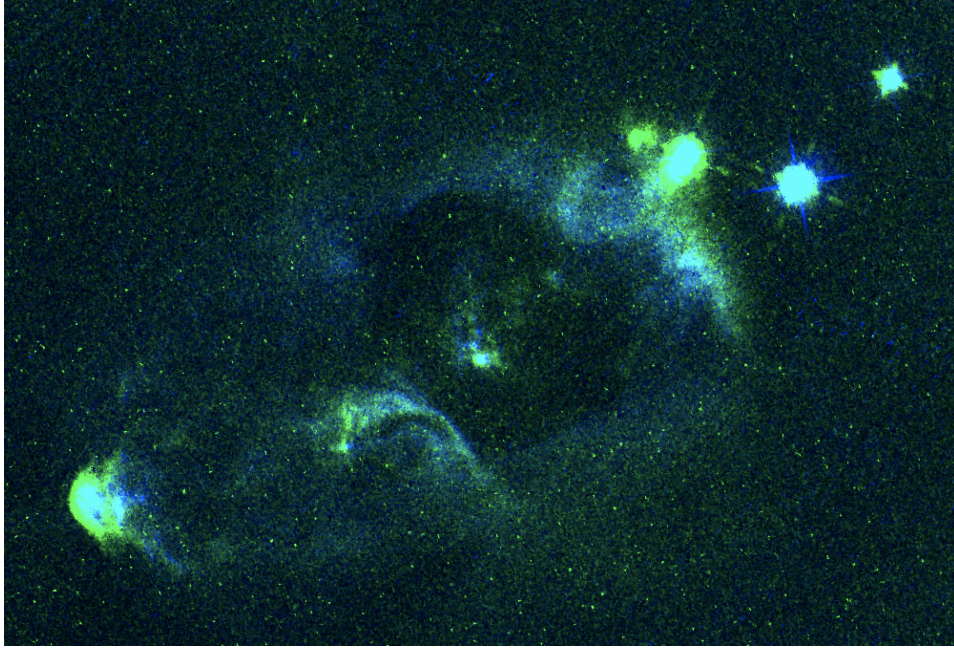


Figure 9. HH 7-11 shown in the SDSS z' continuum filter (green) and H I $\text{Pa}\beta$ (blue). As the stars are emitting in $\text{Pa}\beta$, the areas that are visible in the continuum filter are likely to be continuum contaminated, which is corrected for later in this work.

appears to be lying in the middle of the cavity that HH 8 and HH 9 are on the edge of, as can be seen in Figure 8.

$\text{H}\alpha$ is strong right at the front of the object along the whole length, much wider than where the $\text{Pa}\beta$ emission is but not encompassing the whole size of that covered by $[\text{Fe II}]$. $[\text{S II}]$ covers almost exactly the same area as $[\text{Fe II}]$. H_2 is also in the same approximate area, but in a more rounded shape nearer to the back of the structure, and doesn't reach all the way northwest that the other lines did.

3.1.5. *HH 11*

Similar to HH 9, HH 11 seems mostly devoid of $\text{Pa}\beta$ emission. However, there is possibly a few small sections in the middle, which would line up with the line created from the star to the areas of $\text{Pa}\beta$ emission in HH 10, 8 and 7. It is difficult to tell the significance of the flux though. In the $[\text{Fe II}]$ emission, it shows up strongly, and appears in an arc like shape with a line of emission leading up to the front. There is also no H_2 emission, in fact there almost seems like a cavity in H_2 emission

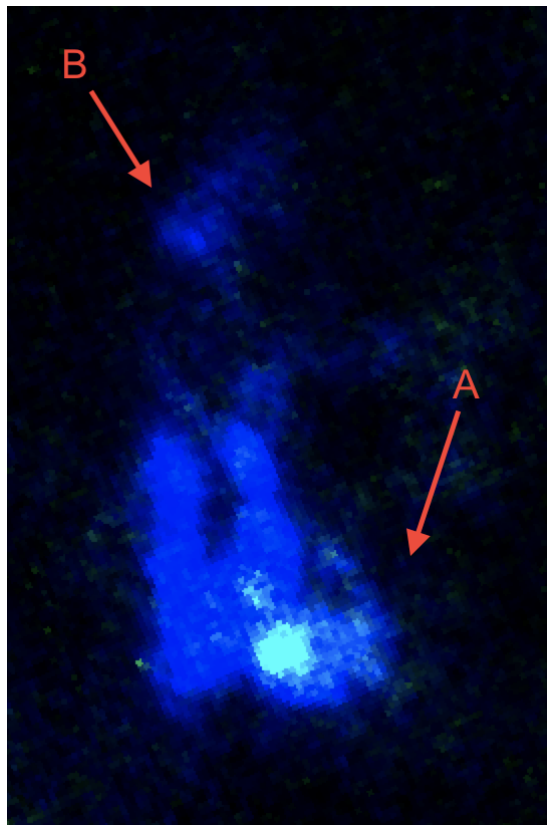


Figure 10. HH 10 shown in [Fe II] 1.26 μm (blue) and H I Pa β 1.28 μm (green). Two structures are labeled: the main structure that is bright in both lines (A), and the more diffuse iron structure (B).

where HH 11 is, although there is emission leading right up to the space. It is quite bright in H α even though it has essentially no Pa β emission. As Pa β is the highest energy tracer available, this is likely to mean that this object reaches a lower shocked temperature in comparison to its counterparts further east. [S II] is visible in the same area as [Fe II].

4. ANALYSIS

4.1. *Foreground Extinction and Continuum Correction*

The 1.64 and 1.26 μm [Fe II] lines are the $a^4D J = 7/2 \rightarrow a^4F J = 9/2$ and $a^4D J = 7/2 \rightarrow a^6D J = 9/2$ transitions, which means that they originate in the same upper state. Because of this, their emitted flux should simply be proportional to the ratio of their Einstein A transition probability coefficients. Thus, if the observed flux differs from this expected emitted flux, this difference can be taken to be directly related to the amount of foreground extinction that lies between us and the

object being observed. In practice, the extinction can only be determined with accuracy sufficient for our purposes in regions where the [Fe II] lines are detected with $S/N > 10$, i.e. within the brightest regions or in large apertures that capture sufficient flux. For these regions, the relation is

$$A_v = 23.6 \log \left(R \frac{f(1.64)}{f(1.26)} \right) \quad (1)$$

where R is that expected relation that comes from the transitional A coefficients (the dereddened line ratio). This value is under significant contention due to the difficulty of observing forbidden lines, as illustrated for example in [Bautista et al. \(2015\)](#). We first attempt to use the commonly maintained value of 4.83 and 4.65 s^{-1} for the 1.64 and 1.26 μm lines respectively ([Nussbaumer & Storey 1988](#)). However, correcting with this value resulted in negative extinction values in high S/N areas, which is a physical impossibility. This result is shown in [13.a](#). Thus, due to our large data set we decide to find our own dereddened ratio as portrayed by our observations. We adopt a value of 2.27 for the 1.26 to 1.64 μm ratio, which corresponds to the peak turnoff in the empirical distribution functions (EDFs) of our flux ratio data for each of HH 7-11, and also HH 6, another HH object included in the observed mosaic which is shown in [Figure 11](#). We determined the turnoff by averaging the results from fitting elbow points to the EDFs and from inflection points of polynomial spline fits to the EDFs. Using this value along with [Equation 1](#) results in [Figure 13.b](#). However, in addition to extinction, the data is also contaminated from continuum emission due to the dust in the area, which acts as an artificial brightening of flux in comparison to the true line emission. This means that the extinction calculation above cannot be simply used, as the continuum must first be corrected for in order for the dereddened ratio method to truly work. But the two are entwined such that one must be known to find the other using this method. Thus, we must solve for both simultaneously.

The continuum emission is strongest in the areas which are visible around the cavity surrounding HH 10, as can be seen in [Figures 8 and 9](#). Dust emits as a diluted blackbody with some characteristic temperature T . As the tail behind HH 8 (C) is pure continuum emission with no line emission, a blackbody spectrum can be fit to this flux to find the characteristic temperature of the blackbody with the typical Planck form

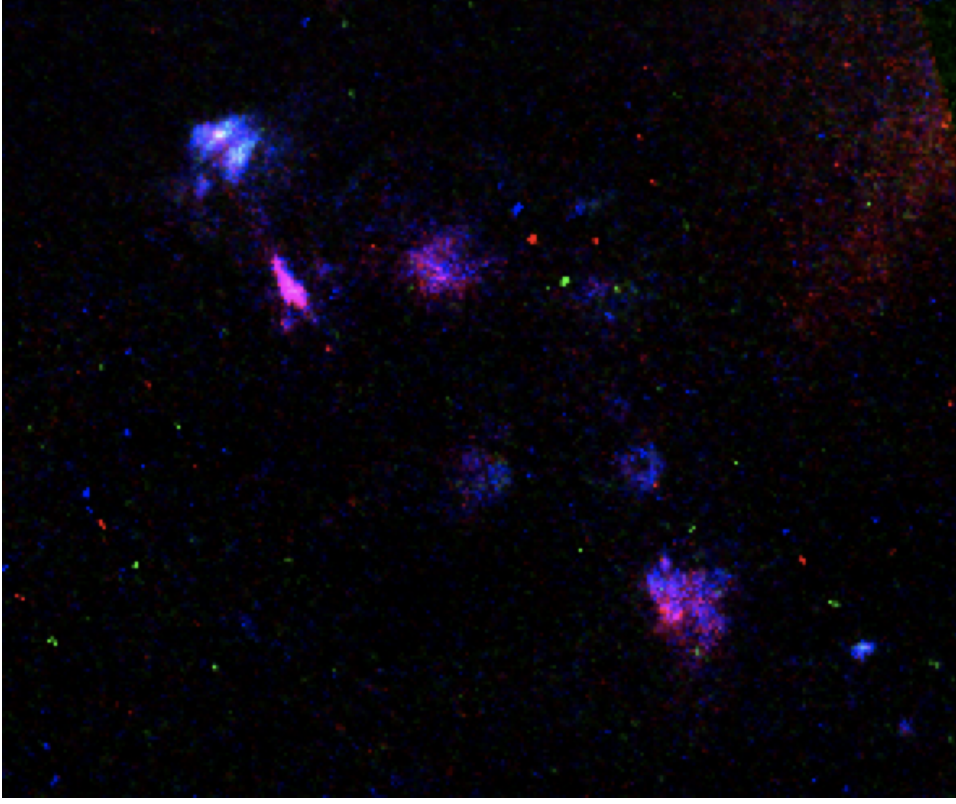


Figure 11. HH 6 shown in [Fe II] 1.26 μm (blue), H I Pa β 1.28 μm (green), and [Fe II] 1.64 μm (red).

$$B_{\lambda}(T) = \frac{2hc^2}{\lambda^5} \frac{1}{e^{hc/\lambda k_B T} - 1} \quad (2)$$

where h is the Planck constant, c is the speed of light, k_B is the Boltzmann constant, and λ is the wavelength of the emission. We use a typical blackbody with temperature $T = 4500$ K. The continuum will always act as an additional flux that needs to be subtracted from the true flux, after an extinction correction. As we have two sets of lines with a required and known dereddened ratio (A similar calculation can be done with hydrogen recombination lines as was done for [Fe II], such as with the two we have data for: H α and Pa β), a system of four equations with four unknowns can be constructed from the observed fluxes (numbered from shortest to longest wavelength - 1: 0.656 μm , 2: 1.26 μm , 3: 1.28 μm , 4: 1.64 μm):

$$f_1 = [R_H f_H + C B_{\lambda}(\lambda_1 T) \Delta \lambda_1] y_1^{A_v} \quad (3)$$

$$f_2 = [R_{Fe} f_{Fe} + C B_{\lambda}(\lambda_2 T) \Delta \lambda_2] y_2^{A_v} \quad (4)$$

$$f_3 = [f_H + CB_\lambda(\lambda_3 T)\Delta\lambda_3] y_3^{A_v} \quad (5)$$

$$f_4 = [f_{Fe} + CB_\lambda(\lambda_4 T)\Delta\lambda_4] y_4^{A_v} \quad (6)$$

where $R_H = 17.5$ is the zero-extinction flux ratio of the $H\alpha$ and $Pa\beta$ lines, $R_{Fe} = 2.23$ is the zero-extinction flux ratio of the $1.64 \mu\text{m}$ and $1.26 \mu\text{m}$ [Fe II] lines, f_H is the extinction corrected Hydrogen flux, f_{Fe} is the extinction corrected [Fe II] flux, A_v is the extinction correction, C is a scale factor that represents the continuum emission predominantly from scattered starlight, and the extinction factors $y_1 - y_4$ are as follows, from the Milky Way dust models of [Weingartner & Draine \(2001\)](#):

$$\text{Extinction} = e^{-\tau} = e^{-zA_v} = y^{A_v} \rightarrow \quad (7)$$

$$y_1 = e^{-0.74982} = 0.47245, \quad y_2 = e^{-0.25739} = 0.77307$$

$$y_3 = e^{-0.24827} = 0.78015, \quad y_4 = e^{-0.16251} = 0.85001$$

The zero-extinction flux ratio of $H\alpha$ to $Pa\beta$ is for a characteristic temperature of $T = 10,000$ K ([Hummer & Storey 1987](#)), which is typical for post-shock regions that emit strongly in H recombination lines. In addition, it is only weakly temperature dependent such that relatively small deviations from this temperature will not cause large changes to the ratio. This system of nonlinear equations is solved for using a Newton-Krylov method root finder using the package SciPy in Python. Prior to finding the roots, the images were smoothed with a 16×16 pixel binning, in order that computation time on a single-core computer was not prohibitive. However, the images are planned to be processed at full resolution once the correct regime is identified to reduce computing time.

The raw observed flux values of 1.26 and $1.64 \mu\text{m}$ [Fe II], and $1.28 \mu\text{m}$ $Pa\beta$ and $0.656 \mu\text{m}$ $H\alpha$, that are used for the extinction and continuum correction calculation are given in [Table 2](#). The regions labeled are as defined in [Figure 12](#).

Included in [Table 3](#) is the values of extinction found for each HH object found using the above relations. The extinction map from these solutions is shown in [Figure 13.c](#), and the extinction contours taken from this data mapped on top of the emission flux is shown in [Figure 13.d](#). From the extinction, it appears that SVS 13 lies almost precisely halfway through the cloud, and the outflow

Table 2. Observed line fluxes^a

	HH 7 (bow)	HH 7 (rest)	HH 8	HH 9	HH 10	HH 11
[Fe II] 1.644 μm	1.10E-13	1.88E-13	1.03E-13	9.72E-15	1.36E-13	4.49E-14
H I Pa β 1.282 μm	5.21E-14	3.37E-14	2.48E-14	1.72E-15	1.81E-14	3.24E-15
[Fe II] 1.257 μm	1.28E-13	1.60E-13	7.56E-14	7.93E-15	1.11E-13	3.33E-14
H I H α 0.656 μm	7.05E-15	1.08E-14	7.49E-15	6.50E-16	9.88E-15	3.72E-15

^aUnits of $\text{erg}/\text{s}/\text{cm}^2$

NOTE—Regions are as defined and shown in Figure 12.

Table 3. Extinction Values

	HH 7 (bow)	HH 7 (rest)	HH 8	HH 9	HH 10	HH 11
A_v	4.91	9.23	11.38	10.05	10.45	11.3

NOTE—Regions are as defined in Figure 12.

is coming out of the cloud towards the surface as generally the A_v values are decreasing from HH 11 to HH 7. HH 11 likely lies a little in front of SVS13. However, HH 10 and HH 9 have a smaller extinction than the surrounding regions, which fits well with the interpretation of the cavity seen in Figure 8 as described previously. The extinction then rises to about the same value for HH 8 on the other side of the cavity, but then decreases throughout HH 7 until it culminates at its bow almost 7 magnitudes less extinguished than HH 11.

The rest of the discussion in this work will be done with data corrected for the extinction as reported.

4.2. MAPPINGS

We use the program MAPPINGS 5.1 to model the HH objects in this region. MAPPINGS is a J-type shock and photoionization modeling program that performs 1D radiative transfer calculations given initial conditions and outputs predicted emission spectra. We use the MAPPINGS 5 code (Allen et al. 2008; Sutherland et al. 2013), running the CHIANTI atomic database (Dere et al. 1997;

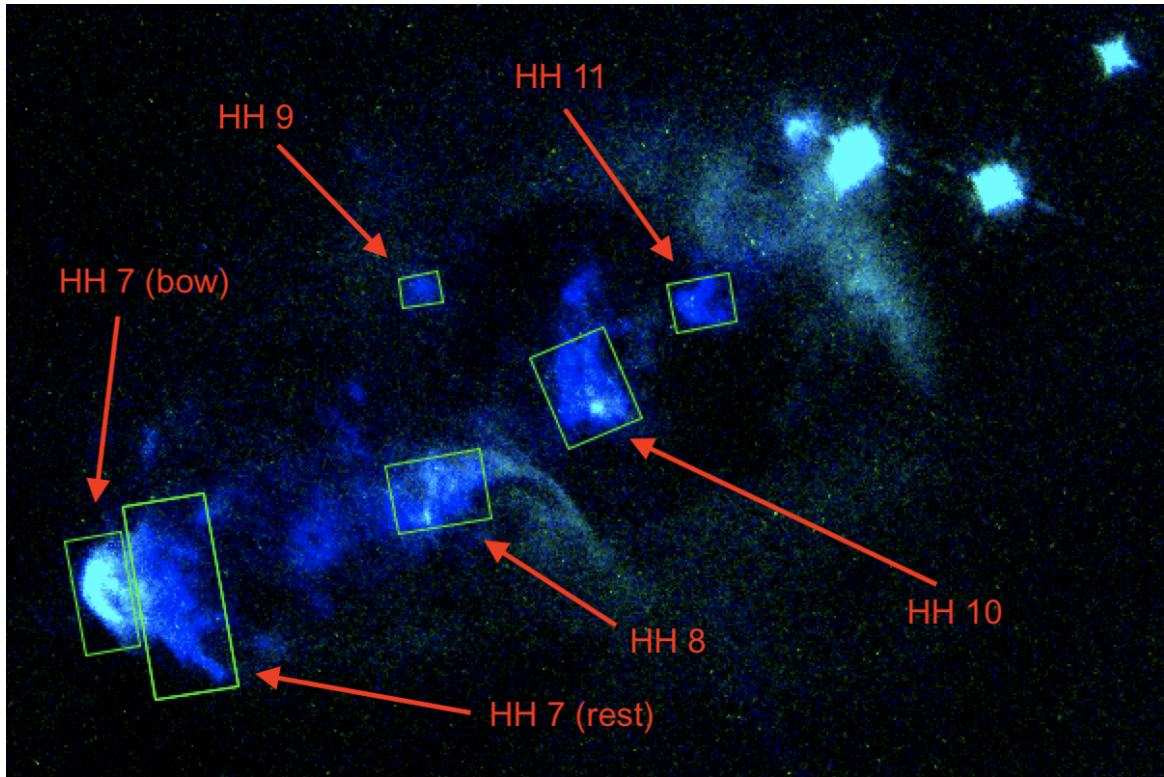


Figure 12. The regions as defined and used for flux collection to use for extinction calculations and modeling. The base image is the same as Figure 3, with $1.28 \mu\text{m}$ H I Pa β (green) and $1.26 \mu\text{m}$ [Fe II] (blue).

Landi et al. 2013) with an adjustment to the [Fe II] rate coefficients to instead be as described in Ramsbottom et al. (2007), to create shock models. In particular, we use the model type S5, which is defined as a shock with adaptive mesh that allows self-preionisation, and we choose to use default ionisation-balance values. The model's default is solar abundance, to which we changed the Fe and Si abundance according to Watson et al. (2016). We use a Maxwellian thermal distribution for the electron energy distribution, and do not include dust physics. We do not add any external photoionisation sources, and do not include cosmic ray heating. We choose to vary the grid regularly in velocity and density, and define a magnetic field at the shock front. The density is tied to the magnetic field strength by the relation

$$B = B_0 \left(\frac{n}{n_0} \right)^{1/2} \quad (8)$$

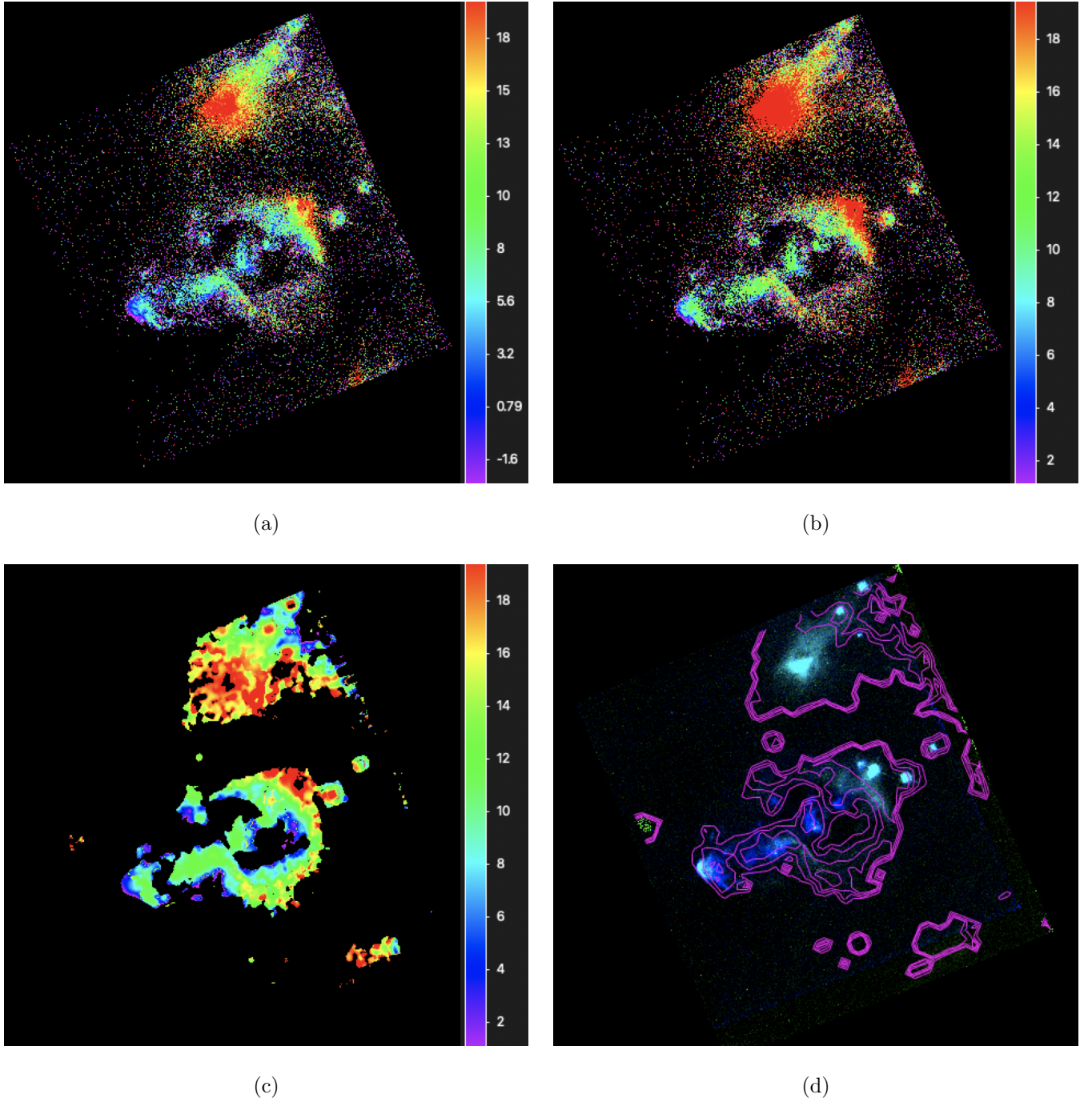


Figure 13. Extinction, given in units of A_v , for the HH 7-11 flow. a: Using the Nussbaumer & Storey (1988) transition coefficient dereddened line ratio. Note the negative extinction values, particularly around the edges of the HH objects. b: Using the 2.23 zero-extinction flux ratio from our data set. Note the lack of spurious negative extinction. c: Using the solutions to the system of Equation 3 to Equation 6. Note that the image is smoothed with a 16x16 pixel binning. d: Contours from c. (3.5, 7, 10.5, 14) plotted on top of the 1.28 μm Pa β and 1.26 μm [Fe II].

Table 4. Extinction and Continuum Corrected Observed Line Fluxes^a

	HH 7 (bow)	HH 7 (rest)	HH 8	HH 9	HH 10	HH 11
[Fe II] 1.644 μm	1.73E-13	1.96E-12	1.04E-12	7.57E-14	1.75E-12	5.26E-13
H I Pa β 1.282 μm	4.80E-13	1.97E-12	1.05E-12	7.28E-14	1.77E-12	4.52E-13
[S II] .672 μm	9.76E-12	7.74E-11	3.32E-11	2.80E-12	7.8E-11	1.74E-11

^aUnits of $\text{erg}/\text{s}/\text{cm}^2$

NOTE—Regions are as defined and shown in Figure 12.

where $B_0 = 50 \mu\text{G}$ and $n_0 = 10,000 \text{ cm}^{-3}$. The exponent 1/2 is how frozen fields scale with density in plane parallel media, with B perpendicular to the flow, with conditions as in the 1D shock models we use (see e.g. [Hollenbach & McKee 1989](#)). We run the models with full diffuse field interaction, and end the simulation when the shocked region reaches a cooled temperature of 100K. We run the shock through three iterations to account for preionization due to ultraviolet self-illumination generated by the shock itself. The first iteration does not include this flux, and so subsequent integrations through the conditions are needed to catch it. After three iterations it was found to converge to a common value such that no further iterations change it. Using observed, corrected line intensities, reported in Table 4, a comparison to the predicted emission lines can be made. From the corrections, only one of [Fe II] 1.64 μm and 1.26 μm , and one of H α and Pa β is used, as they are degenerate following the previous corrections made in Section 4.1. We will use [Fe II] 1.64 μm Pa β 1.28 and μm , and the [S II] 0.672 μm line to do high resolution simulation matching. This is done using chi-squared minimization of the form

$$\chi^2 = \sum \frac{F - (M * S)}{U} \quad (9)$$

where the sum is over all of the lines being matched, F is the observed flux, M is the predicted model's flux, S is a scale factor added in to account for a variety of factors due to observation variables such as the beam-filling factor (the fraction of a pixel's solid angle that is filled with emitting material), and U is the uncertainty in the observation. This is implemented with code written in Python.

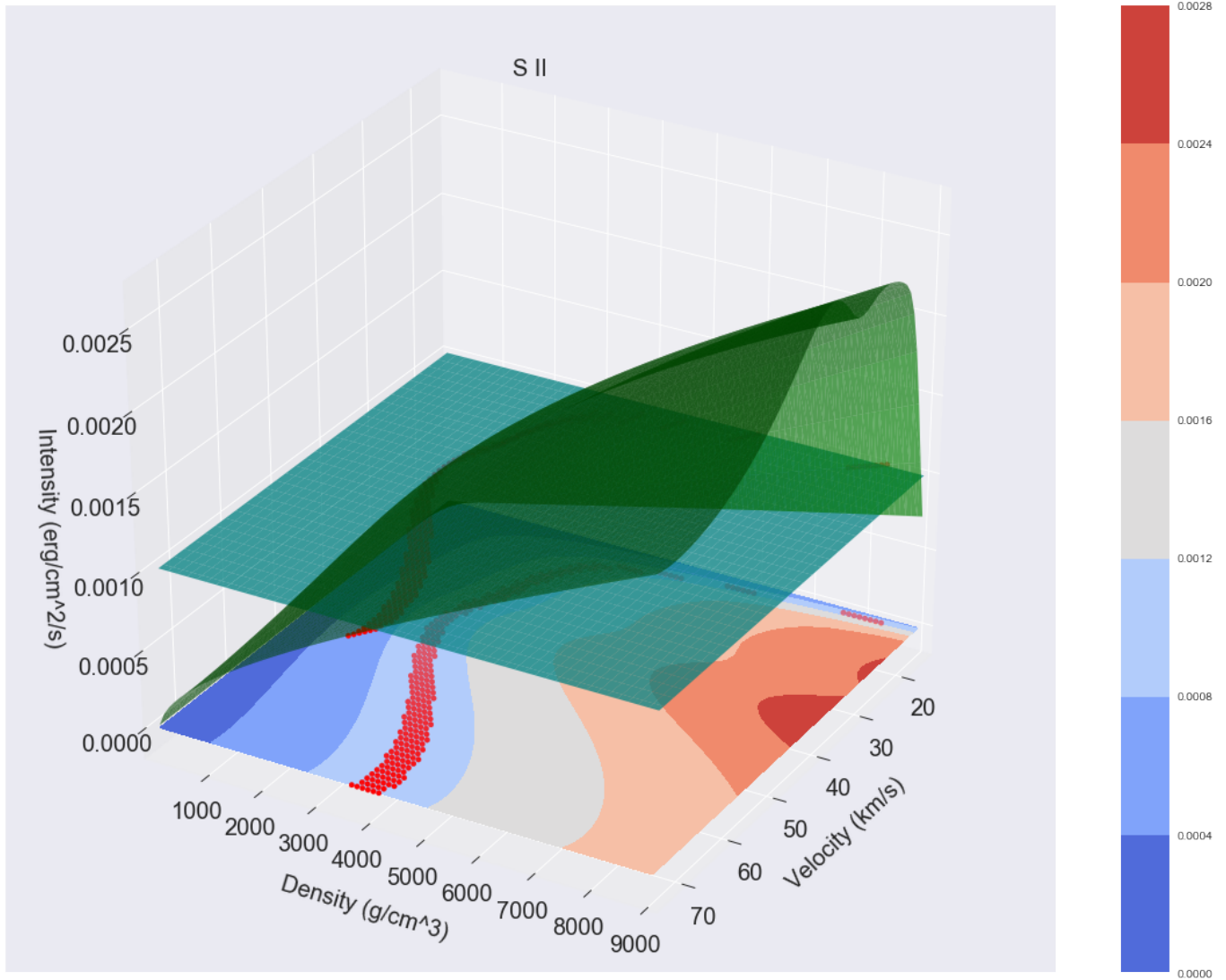


Figure 14. A 3D plot illustrating the matching of observed and simulated intensities of the flux of [S II]. The green surface is the [S II] flux as predicted by the MAPPINGS V shock simulation corresponding to some initial velocity and density, while the teal plane is the flux as observed by HST, appropriately scaled. Plotted on the x-y axis is a contour plot projection of the green surface, mapped to the color bar on the right. The red dots correspond to the points that the intersection of the surfaces within the uncertainties of the observations. These points are also projected onto the x-y axis contour plot.

4.2.1. Modeling

The results of our models are shown in Table 5. A plot showing the behavior of one of the simulated lines, as an example of how the matching is done, is shown in Figure 14.

Table 5. Modeling Results

	Chisquared (unreduced)	Velocity (km/s)	Density (cm^{-3})	Magnetic Field (μG)	Scale Factor
HH 7 (bow)	8.7	60	125,000	176.8	8.50E-12
HH 7 (rest)	8.9	61	100,000	158.1	4.68E-11
HH 8	7.9	61	100,000	158.1	2.48E-11
HH 9	8.3	60	100,000	158.1	1.83E-12
HH 10	9.1	61	100,000	158.1	4.19E-11
HH 11	7.6	58	275,000	262.2	1.54E-11

NOTE—Regions are as defined and shown in Figure 12.

There are two main theories regarding how outflows form: a continuous stream of material or repeated short burst events that eject material. The simulation results seem to point to the second of those theories, that the variables that best matched the majority of HH objects in this object are due to some characteristic accretion event that happens regularly and repeatedly. Note that it is also possible to get these types of HH objects from internal shock mechanics, which may fit more strongly with the observed proper motions (Hartigan et al. 2019).

4.2.2. Derived Quantities

We can calculate parameters of feedback given the the observational data and the modeling results found above. As derived in Watson et al. (2016), the mass flow rate is

$$\dot{M}_w = 1.4 \times 10^{-3} L([\text{Fe II}] 26.0 \mu\text{m}) \frac{M_{\odot} \text{year}^{-1}}{L_{\odot}} \quad (10)$$

We can use the 26.0 μm [Fe II] line as predicted using the MAPPINGS V simulation for this equation to find the mass flow rate value. Multiplying the this flux by the scaling relation found in the matching process will give an accurate starting point, which is then must be multiplied by the area of the emitting region to find the emitted power:

$$L([\text{Fe II}] 26 \mu\text{m}) = f([\text{Fe II}] 26 \mu\text{m}) S \times \Omega d^2 \quad (11)$$

where f is the flux, S is the scale factor, $\Omega = 4\pi$ is the solid angle of the emitting region and d is the distance ($d = 300$ pc as stated previously). This is the value that will be used in the equation above.

Table 6. Derived Rates

	L(26.0 μm [Fe II])	Mass Flow Rate	Momentum Injection	Kinetic Energy Injection
	(ergs/s)	(M_{\odot} /year)	Rate (dynes)	Rate (ergs/s)
HH 7 (bow)	2.0E31	7.2E-6	2.7E27	8.2E33
HH 7 (rest)	9.0E31	3.3E-5	1.3E28	3.9E34
HH 8	4.7E31	1.8E-5	6.9E27	2.1E34
HH 9	3.4E30	1.3E-6	4.9E26	1.5E33
HH 10	8.0E31	2.9E-5	1.1E28	3.4E34
HH 11	1.2E31	4.4E-6	1.6E27	4.7E33
Total	4.7E41	9.3E-5	3.6E28	1.1E35

NOTE—Regions are as defined and shown in Figure 12.

Using this rate, we can also find the momentum and kinetic energy injection rates:

$$\dot{p} = \dot{M}_w v_s \quad (12)$$

$$\dot{KE} = \frac{1}{2} \dot{M}_w v_s^2 \quad (13)$$

where v_s is the speed of the shock as found by the simulation. We find these three quantities for each of the regions as were simulated in Section 4.2 and show the results in Table 6.

4.3. Larger Scale Structure

4.3.1. Molecular Hydrogen C-Type Shock

While the HH regions are showing the J-type wind shock, there is also a larger structure around this due to the C-type cloud shock. This is visible in a variety of molecular Hydrogen lines observed with Spitzer. An example of this is shown in Figure 15.a. Unlike the sophisticated and computationally expensive modeling required for the simulation of J-type shocks due to the extensive number of varied lines emitted by the shock, C-type shocks can be treated more simply. The pure rotational molecular Hydrogen lines contain more than half of the cooling power of all lines emitted by the C-type shock (Maret et al. 2009), and thus are able to accurately predict outcomes themselves. In Table 7, we show

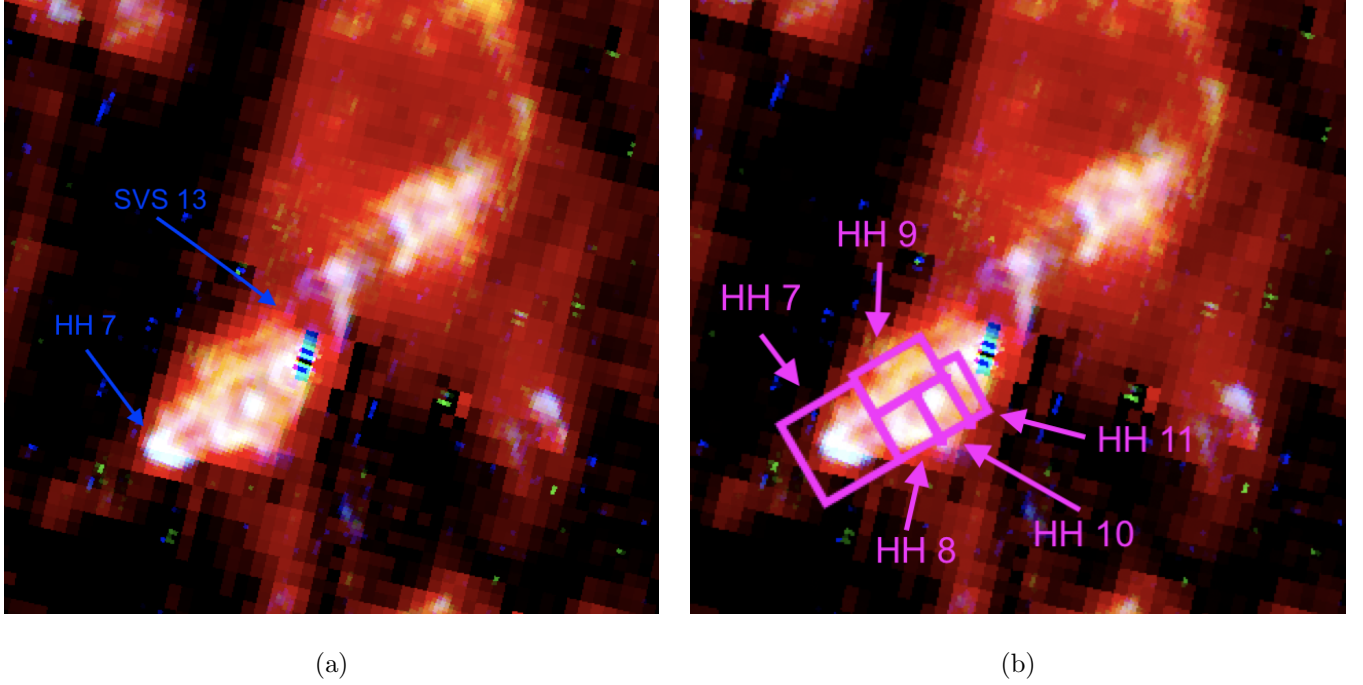


Figure 15. a: Spitzer images of the region around HH 7-11, with SVS 13 and HH 7 labeled for reference. Red: H_2 S1, Green: H_2 S3, Blue: H_2 S5. The larger scale structure, including a flow on the opposite side of HH 7-11, is seen. b: The regions used for the collection of molecular hydrogen flux. These are different than the regions used previously due to the differences in resolution.

molecular hydrogen values obtained from the Spitzer observations. Note that the regions defined for these flux values is different than was used previously, and are shown in Figure 15.b.

If the sum of this molecular hydrogen flux is taken and multiplied by two, and multiplied by the area of the emitting region like as was done in Section 4.2.2, we are able to obtain a proxy for the total cooling power of the C-type shock, and thus the turbulent energy being deposited by it. These results are shown in Table 8.

4.3.2. Potential Counterjet

The region that would contain a counterjet is shown in Figure 16. The only emission seen in these HST lines is a few nebulous areas of [Fe II]. As it seems from the extinction values calculated that the outflow that created HH 7-11 is starting near the middle of the cloud and reaching towards the surface, it is likely that the counterjet is deeply embedded into the cloud. Thus, the only chance to

Table 7. Molecular Hydrogen Fluxes ^a

	HH 7	HH 8	HH 9	HH 10	HH 11
H_2 S(0)	1.22E-13	5.16E-14	6.49E-14	3.25E-14	2.49E-14
H_2 S(1)	9.72E-13	6.42E-13	8.50E-13	3.32E-13	4.53E-13
H_2 S(2)	2.46E-12	6.97E-13	8.23E-13	3.59E-13	2.17E-13
H_2 S(3)	2.45E-12	1.37E-12	1.75E-12	9.77E-13	6.56E-13
H_2 S(4)	2.03E-12	4.63E-13	4.79E-13	3.68E-13	2.46E-13
H_2 S(5)	2.93E-12	1.49E-12	1.34E-12	9.92E-13	6.80E-13
H_2 S(6)	1.07E-12	3.26E-13	1.38E-13	1.62E-13	7.71E-14
H_2 S(7)	2.57E-12	1.01E-12	1.01E-12	7.86E-13	6.02E-13

^aUnits of $erg/s/cm^2$

NOTE—Regions are as defined and shown in Figure 15.b. Note that these regions are different than those previously used due to the significant difference in resolution between the observing modes.

Table 8. C-Type Shock Cooling Power ^a

	HH 7	HH 8	HH 9	HH 10	HH 11	Total
Total Flux ($erg/cm^2/s$)	1.17E-12	6.48E-13	8.17E-13	4.78E-13	4.27E-13	3.54E-12
Cooling Power (ergs/s)	1.3E31	7.0E30	8.8E30	5.2E30	4.6E28	3.8E31

^aUnits of $erg/s/cm^2$

NOTE—Regions are as defined and shown in Figure 15.b. Note that these regions are different than those previously used due to the significant difference in resolution between the observing modes.

observe it is in the longer wavelength lines taken with Spitzer, not HST. There is strong emission in the Spitzer data that corresponds to this region. Firstly, as stated and shown above in Figure 15, there is significant molecular Hydrogen emission in the whole region opposite the main HH 7-11 flow. In addition, there is emission that seems that it could be opposite HH 7 in [Fe II] and [Si II] data from the LH filter, but further reduction and analysis must be carried out to determine its significance.



Figure 16. Both sides of SVS 13, with $1.64 \mu\text{m}$ [Fe II] in red, $1.28 \mu\text{m}$ H I Pa β in green, and $1.26 \mu\text{m}$ [Fe II] in blue.

Symmetric structures on opposite sides of a source are implications for the jet and counterjet having synchronized ejections, which may allow for further constraint on the jet production region, as was explained by [Raga et al. \(2011a\)](#) for HH 34. As there are long-standing questions about the jet launching and collimation mechanisms, what this symmetric structure can tell us about the source region may help find some answers.

4.4. *Turbulent Energy Implications*

If the energy values for the J-type and C-type shocks found above are taken as typical, and thus assumed to be approximately the values representative of each outflow in NGC 1333, we can find the total turbulent energy injection rate for the cloud as a whole. We observe 17 outflows in the region, which needs to be multiplied by 2 to account for the counterjet energy. As the average lifetime of a stellar outflow is on the order of 1,000 - 10,000 years ([Raga et al. 2013](#)), this can be multiplied against the injection rates to find a range of likely values over the lifetime of the outflows.

From the total extinction derived from star counts, we know that the total binding energy of NGC 1333 is about 10^{46} ergs (Gutermuth et al. 2008). Comparing this to the energy injection over the lifetime of the outflows, we find that the total turbulent energy is

$$\text{Turbulent Energy} = (1.1E35 + 3.8E31) \text{ ergs/cm}^2/\text{s} \times 17 \times 2 \times 1000 \text{ years to} \quad (14)$$

$$(1.1E35 + 3.8E31) \text{ ergs/cm}^2/\text{s} \times 17 \times 2 \times 10000 \text{ years} \rightarrow$$

$$\text{Turbulent Energy} = 1.2 \times 10^{47} - 1.2 \times 10^{48} \text{ ergs}$$

This is larger than the total binding energy of the cloud even for the shorter lifetime, and thus in this case the outflows would be able to disrupt the cloud by overcoming its binding energy. However, HH 7-11 is a very powerful outflow, and thus it is significantly possible that this is an overestimate of the average outflow strength in the cloud.

5. CONCLUSION

We have shown high resolution HST images of the objects contained in the outflow of SVS13, HH 7-11. This high resolution imagery has allowed for a variety of morphological arguments, including showing interesting structure such as the two shock fronts of HH 7. In addition, we have been able to conclude that the HH 7-11 region is significantly contaminated by high extinction regions and continuum due to dust scattered starlight, and so our view of this region thus far has been skewed by this fact, especially in the shorter wavelength regimes. The behavior of this extinction also seems to show that SVS13 is deeply embedded in its cloud, starting almost precisely halfway through with its outflow plowing out of the cloud towards the front. We have also shown initial modeling results using a variety of extinction and continuum corrected HST lines which show the evolution of the shock along its path towards HH 7, and seem to be evidence of regular, repeated accretion events that eject outflows. We looked at the total turbulent energy being deposited by both the J-type and C-type shock in HH 7-11 and concluded that if the values were characteristic and true for all of the 17 shocks in the regions and their counterjets, the total injected energy and momentum would be large enough to overcome the binding energy and disrupt the cloud. However, HH 7-11 is a very

strong outflow and so it is likely an overestimate of the total power. More research will need to be done before a true determination of the eventual future of the cloud can be made.

There is still significant future work still planned for this project and data. In the near future, the Spitzer emission lines will be added to those from HST to do more robust simulation modeling of the HH objects, albeit at a lower resolution. Additionally, this is the first project completed using the new HST data mosaic, and thus the rest of the region still remains to be explored. This method of simulation matching will eventually be carried out for all the outflows in the region so that a more solid determination of the total momentum and energy injection rates can be made, and the future of this cloud can be deduced more conclusively.

This work is based in part on observations made with the NASA/ESA Hubble Space Telescope, obtained from the data archive at the Space Telescope Science Institute. STScI is operated by the Association of Universities for Research in Astronomy, Inc. under NASA contract NAS 5-26555. These observations are associated with program #15153 and program #15257. This work is based in part on observations made with the Spitzer Space Telescope, which is operated by the Jet Propulsion Laboratory, California Institute of Technology under a contract with NASA. This publication makes use of data products from the Two Micron All Sky Survey, which is a joint project of the University of Massachusetts and the Infrared Processing and Analysis Center/California Institute of Technology, funded by the National Aeronautics and Space Administration and the National Science Foundation. CHIANTI is a collaborative project involving George Mason University, the University of Michigan (USA), University of Cambridge (UK) and NASA Goddard Space Flight Center (USA). This research has made use of the SIMBAD database, operated at CDS, Strasbourg, France. The UKIDSS project is defined in [Lawrence et al. \(2007\)](#). UKIDSS uses the UKIRT Wide Field Camera (WFCAM; [Casali et al. 2007](#)). The photometric system is described in [Hewett et al. \(2006\)](#), and the calibration is described in [Hodgkin et al. \(2009\)](#). The pipeline processing and science archive are described in [Irwin et al \(2020, in prep\)](#) and [Hambly et al. \(2008\)](#).

REFERENCES

- Allen M. G., Groves B. A., Dopita M. A., Sutherland R. S., Kewley L. J. 2008, *ApJS*, 178, 20
 Anglada, G., Rodríguez, L.F., & Torrelles, J.M., 2000, *ApJ*, 542, L123

- Bachiller, R., Gueth, F., Guilloteau, S., Tafalla, M., & Dutrey, A. 2000, *A&A*, 362, L33
- Bally, J., 2016, *ARA&A*, 54, 491
- Barth A. J., 2001, in Harnden F. R., Jr, Primini F. A., Payne H. E., eds, *ASP Conf. Ser. Vol. 238, Astronomical Data Analysis Software and Systems X*. Astron. Soc. Pac., San Francisco, p. 385
- Bautista, M. A., Fivet, V., Ballance, C., et al. 2015, *ApJ*, 808, 174
- Casali, M. et al., 2007, *A&A*, 467, 777
- Cutri, R. M., et al. 2006, *Explanatory Supplement to the 2MASS All Sky Data Release and Extended Mission Products*, www.ipac.caltech.edu/2mass/releases/allsky/doc/explsup.html
- Dere, K. P., Landi, E., Mason, H. E., Monsignori Fossi, B. C., & Young, P. R. 1997, *A & A Supplement series*, 125, 149
- Draine, B. T. 1980, *ApJ*, 241, 1021
- Dressel, L., 2019 “Wide Field Camera 3 Instrument Handbook, Version 11.0” (Baltimore: STScI)
- Frank, A., Ray, T. P., Cabrit, S., et al. 2014, in *Protostars and Planets VI*, ed. H. Beuther et al. (Tucson, AZ: Univ. Arizona Press), 451
- Gardner J. P., et al., 2006, *SSRv*, 123, 485
- Gonzaga, S., Hack, W., Fruchter, A., Mack, J., eds. 2012, *The DrizzlePac Handbook*. (Baltimore, STScI)
- Gutermuth, R. A., Myers, P. C., Megeath, S. T. et al. 2008, *ApJ*, 674, 336
- Hambly, N. C. et al., 2008, *MNRAS*, 384, 637
- Hartigan, P. et al. 2019. *ApJ*, 876, 147
- Herbig, G. 1974, *Lick Obs. Bull. No. 658*
- Herbig, G. H., & Jones, B. F. 1983, *AJ*, 88, 1040
- Hewett, P. C., Warren, S. J., Leggett, S. K., & Hodgkin, S. T. 2006, *MNRAS*, 367, 454
- Hodapp, K.W., & Chini, R. 2014, *ApJ*, 794, 169
- Hodgkin, S. T., Irwin, M. J., Hewett, P. C., & Warren, S. J. 2009, *MNRAS*, 394, 675
- Hollenbach, D., & McKee, C. F. 1989, *ApJ*, 342, 306
- Houck, J. R., Roellig, T. L., van Cleve, J., et al. 2004, *ApJS*, 154, 18
- Hummer, D. G. & Storey, P. J. 1987, *MNRAS*, 224, 801
- Khanzadyan, T., Smith, M. D., Davis, C. J., et al. 2003, *MNRAS*, 338, 57
- Landi, E., Young, P. R., Dere, K. P., Del Zanna, G., & Mason, H. E. 2013, *ApJ*, 763, 86
- Lawrence, A. et al., 2007, *MNRAS*, 379, 1599
- Maret, S., Bergin, E. A., Neufeld, D. A., et al. 2009, *ApJ*, 698, 1244
- Momcheva, I. G. et al. 2017. *PASP*, 129, 015004
- Neufeld, D. A., Melnick, G. J., Sonnentrucker, P., et al. 2006, *ApJ*, 649, 816
- Neufeld D. A., Hollenbach D. J., Kaufman M. J., Snell R. L., Melnick G. J., Bergin E. A., Sonnentrucker P., 2007, *ApJ*, 664, 890
- Noriega-Crespo, A. & Garnavich, P. M. 2001, *AJ*, 122, 3317
- Nussbaumer, H., & Storey, P. J. 1988, *A&A*, 193, 327

- Offner, S. S. R., Dunham, M. M., Lee, K. I., Arce, H. G., & Fielding, D. B. 2016, *ApJL*, 827, L11
- Raga, A. C., Noriega-Crespo, A., Lora, V., Stapelfeldt, K. R., & Carey, S. J. 2011a, *ApJ*, 730, L17
- Raga, A. C., Noriega-Crespo, A., Carey, S. J., & Arce, H. G. 2013, *AJ*, 145, 28
- Ramsbottom, C. et al. 2007, *A&A*, 475, 765
- Rodríguez L.F., Anglada G., Curiel S., 1997, *ApJ*, 480, L125
- Reipurth, B.: 1999, *A general catalogue of Herbig-Haro objects*, 2. edition, <http://casa.colorado.edu/hhcat>
- Skrutskie M. F., et al., 2006, *AJ*, 131, 1163
- Smith J. D. T., et al., 2007, *PASP*, 119, 1133
- Solf, J., & Böhm, K.-H. 1987, *AJ*, 93, 1172
- Stapelfeldt, K. R., Scoville, N. Z., Beichman, C. A., Hester, J. J., & Gautier, T. N., III 1991, *ApJ*, 371, 226
- Strom, S. E., Vrba, F. J., & Strom, K. M. 1976, *AJ*, 81, 314
- Sutherland, R. S. et al. 2013. *Astrophysics Source Code Library*, record 1306.008
- Walawender, J., Bally, J., & Reipurth, B. 2005, *AJ*, 129, 2308
- Watson, D. M. et al., 2016, *ApJ*, 828, 52
- Weingartner, J. C., & Draine, B. T. 2001, *ApJ*, 548, 296
- Wilson, R. W., Jefferts, K. B., & Penzias, A. A. 1970, *ApJ*, 161, L43
- Yuan Y. & Neufeld D. A., 2011, *ApJ*, 726, 76
- Zucker, C., Schlafly, E. F., Speagle, J. S., et al. 2018, *ApJ*, 869, 83

APPENDIX

A. ADDITIONAL FIGURES

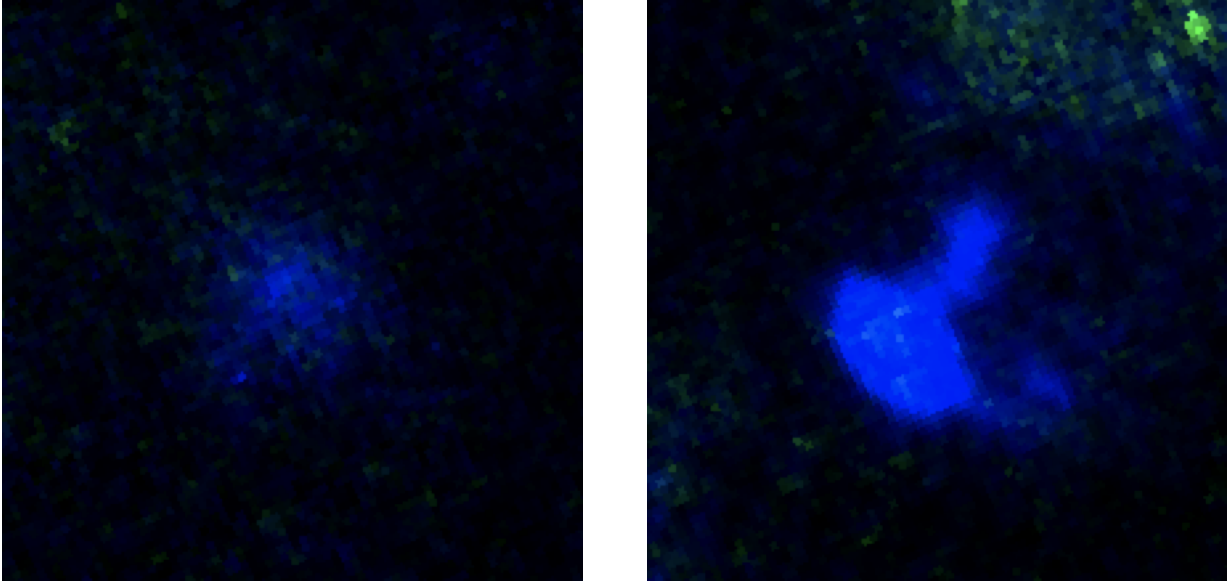


Figure 17. Left: HH 9 shown in [Fe II] 1.26 μm (blue) and 1.64 μm (red). Pa β is also being shown in this image, but HH 8 seems to be completely devoid of it. Right: HH 11 shown in [Fe II] 1.26 μm (blue) and H I Pa β 1.28 μm , although the Pa β is so faint it is difficult to tell if it is significant source or just rogue pixels. Pa β emission that is likely continuum reflection from dust around the star is visible in the upper right but is not a part of the object.